





# Commensal microbiota divergently affect myeloid subsets in the mammalian central nervous system during homeostasis and disease

Roman Sankowski<sup>1,2</sup> , Jasmin Ahmari<sup>1</sup>, Charlotte Mezö<sup>1,3</sup>, Anna Lena Hrabě de Angelis<sup>1</sup>, Vidmante Fuchs<sup>1,3</sup> , Olaf Utermöhlen<sup>4</sup>, Thorsten Buch<sup>5</sup>, Thomas Blank<sup>1</sup>, Mercedes Gomez de Agüero<sup>6</sup> , Andrew J Macpherson<sup>6</sup> & Daniel Erny<sup>1,7,\*</sup> 

## Abstract

The immune cells of the central nervous system (CNS) comprise parenchymal microglia and at the CNS border regions meningeal, perivascular, and choroid plexus macrophages (collectively called CNS-associated macrophages, CAMs). While previous work has shown that microglial properties depend on environmental signals from the commensal microbiota, the effects of microbiota on CAMs are unknown. By combining several microbiota manipulation approaches, genetic mouse models, and single-cell RNA-sequencing, we have characterized CNS myeloid cell composition and function. Under steady-state conditions, the transcriptional profiles and numbers of choroid plexus macrophages were found to be tightly regulated by complex microbiota. In contrast, perivascular and meningeal macrophages were affected to a lesser extent. An acute perturbation through viral infection evoked an attenuated immune response of all CAMs in germ-free mice. We further assessed CAMs in a more chronic pathological state in 5xFAD mice, a model for Alzheimer's disease, and found enhanced amyloid beta uptake exclusively by perivascular macrophages in germ-free 5xFAD mice. Our results aid the understanding of distinct microbiota–CNS macrophage interactions during homeostasis and disease, which could potentially be targeted therapeutically.

**Keywords** Alzheimer's disease; CNS-associated macrophages; LCMV; microbiota; microglia

**Subject Categories** Immunology; Neuroscience

**DOI** 10.15252/embj.2021108605 | Received 28 April 2021 | Revised 7 September 2021 | Accepted 14 September 2021 | Published online 7 October 2021

**The EMBO Journal (2021) 40: e108605**

## Introduction

As innate immune cells in the central nervous system (CNS), tissue macrophages encompass a heterogeneous population of myeloid cells. Microglia are localized in the CNS parenchyma, while the non-parenchymal CNS-associated macrophages (CAMs) reside at the border regions as choroid plexus macrophages (cpMΦ), leptomeningeal macrophages (mMΦ), and perivascular macrophages (pvMΦ) (Prinz *et al*, 2017; Brioschi *et al*, 2020). Despite the fact that these macrophage subsets are generally involved in scavenging of cell debris, pathogens, and molecules, they fulfill distinct region-specific tasks, such as support of neurons and oligodendrocytes by microglia in the brain parenchyma, or vascular remodeling and drainage of toxic protein aggregates by pvMΦ (Zhou *et al*, 2010; Ueno *et al*, 2013; Hawkes *et al*, 2014; Faraco *et al*, 2016; Hagemeyer *et al*, 2017; Herz *et al*, 2017; Kierdorf *et al*, 2019). Recent studies have established that both microglia and CAMs are self-renewing long-living cells with a solely prenatal yolk sac origin. A notable exception is cpMΦ that is replaced by C-C chemokine receptor type 2 (CCR2)-dependent Ly6C<sup>high</sup>-expressing blood-derived monocytes over time analogous to other selected peripheral tissue macrophages (Goldmann *et al*, 2016; Hoeffel & Ginhoux, 2018; Van Hove *et al*, 2019). Recently, it was suggested that, distinct from microglia, development of CAMs occurs independent of transforming growth factor beta (TGF-β) (Utz *et al*, 2020).

In the past, the discrimination of the CNS tissue macrophage subsets was mainly based on the anatomical region. In addition, some markers are specifically expressed either by CAMs or by microglia. Under homeostatic conditions, these include *Mannose receptor C-type 1* (*Mrc1*, encoding CD206), *Cd163*, and *Lymphatic vessel endothelial hyaluronan receptor (Lyve1)* for CAMs or *hexosaminidase subunit beta* (*Hexb*) and *Transmembrane protein 119*

1 Institute of Neuropathology, Faculty of Medicine, University of Freiburg, Freiburg, Germany

2 Berta-Ottenstein-Programme, Faculty of Medicine, University of Freiburg, Freiburg, Germany

3 Faculty of Biology, University of Freiburg, Freiburg, Germany

4 Institute for Medical Microbiology, Immunology and Hygiene & Center for Molecular Medicine Cologne (CMMC), University of Cologne, Koeln, Germany

5 Institute of Laboratory Animal Science, University of Zurich, Zurich, Switzerland

6 Maurice E. Müller Laboratories, Department for Biomedical Research (DBMR), University Clinic of Visceral Surgery and Medicine, Inselspital, University of Bern, Bern, Switzerland

7 Berta-Ottenstein-Programme for Advanced Clinician Scientists, Faculty of Medicine, University of Freiburg, Freiburg, Germany

\*Corresponding author. Tel: +49 761 270 51090; Fax: +49 761 270 50500; E-mail: daniel.erny@uniklinik-freiburg.de

(*Tmem119*) for microglia (Zeisel *et al*, 2015; Goldmann *et al*, 2016; Jordao *et al*, 2019; Van Hove *et al*, 2019; Kim *et al*, 2021). Common myeloid cell markers such as ionized calcium binding adaptor molecule 1 (*Iba1*), *Cd11b*, or Cx3 chemokine receptor 1 (*Cx3cr1*) are expressed by both microglia and CAMs (Prinz *et al*, 2017). Compared to microglia, the biological functions of CAMs are understudied and not yet well understood (Kierdorf *et al*, 2019). It is suggested that CAM subsets are implicated in scavenging cellular debris, pathogens, and molecules (Mrdjen *et al*, 2018; Kierdorf *et al*, 2019). In mouse models of Alzheimer's disease (AD), a critical role of pvMΦ in amyloid beta (Aβ) clearance was reported (Hawkes & McLaurin, 2009; Mildner *et al*, 2011).

It is widely accepted that the microglial identity in the CNS is imprinted by ontogenetic, species- and tissue-specific as well as environmental factors, such as the gut microbiota (Gosselin *et al*, 2014; Lavin *et al*, 2014; Erny *et al*, 2015; Amit *et al*, 2016; Geirsdottir *et al*, 2019; Erny & Prinz, 2020). Previously, we showed that host microbiota control maturation and function of microglia under steady-state and pathological conditions (Erny *et al*, 2015). Mice born and raised in a germ-free (GF) environment, constitutively lacking commensal microbes, exhibited an immature microglial phenotype with altered gene expression profile, increased cell numbers, hyper-ramified morphology, and impaired immune response compared with colonized mice raised under specific pathogen-free (SPF) conditions (Erny *et al*, 2015). Short-chain fatty acids (SCFAs), microbiota-derived fermentation products, were shown to mediate these effects on microglia in homeostatic and disease conditions (Erny *et al*, 2015; Sampson *et al*, 2016; Chu *et al*, 2019; Erny & Prinz, 2020; Mezo *et al*, 2020). Additionally, a microbiota-dependent Aβ uptake by microglia was shown in the 5x familial AD (5xFAD) mouse model for AD (Mezo *et al*, 2020). However, whether all CNS myeloid cells across the CNS are shaped by gut microbiota in the homeostatic and diseased CNS, the underlying transcriptional program on a single-cell level as well as functional implications remained unknown.

Overall, we found an altered transcriptional phenotype of GF-associated CAMs. Notably, we identified predominantly cpMΦ as highly responsive to the GF status. Interestingly, the presence of a complex microbiota was a crucial determinant of the response of

CAMs to an acute viral infection with lymphocytic choriomeningitis virus (LCMV). In a more chronic pathological state in the 5xFAD mouse model of AD, we revealed microbiota-dependent alterations in the Aβ uptake only in pvMΦ. Our results indicate context-dependent specific effects of environmental microbes on selective CNS myeloid cells and thereby modulating CNS immunity.

## Results

### scRNA-seq identifies microbiota-dependent imprints on myeloid subsets in distinct CNS compartments

To assess myeloid cells at single-cell level, we dissected several CNS compartments. Viable CD11b<sup>+</sup>CD45<sup>+</sup>CD3<sup>-</sup>B220<sup>-</sup>Ly6G<sup>-</sup> cells from the parenchyma, choroid plexus, leptomeninges, and perivascular space from SPF and GF mice were fluorescence-activated cell sorting (FACS)-isolated (Fig EV1). Compared to parenchymal microglia, the absolute numbers of CAMs are considerably lower. Therefore, we subjected the isolated myeloid cells to high-throughput single-cell RNA-sequencing (scRNA-seq) using the high-sensitivity method mCEL-Seq2 (Herman *et al*, 2018; Jordao *et al*, 2019; Sankowski *et al*, 2019; Ding *et al*, 2020) followed by analysis using Seurat version 3 (Stuart *et al*, 2019) (Fig 1). After quality control, we assembled a transcriptional atlas comprising a total of 2,745 cells recovered from all CNS compartments of SPF and GF animals (Fig 1A). We represented these data using dimensionality reduction with Uniform Manifold Approximation and Projection for Dimension Reduction (UMAP). To discriminate the main cell types in the CNS, we generated maps for the myeloid cell populations based on published signature genes (Jordao *et al*, 2019) (Fig 1B). Further, the investigated compartment of each cell was displayed in a color-coded UMAP plot (Fig 1C). By using Seurat analysis, we identified 17 molecularly distinct clusters of predominantly innate immune cells from the different CNS compartments (Fig 1D, Table EV1 cell counts per cluster). The majority of cells were attributed as macrophages whereby seven clusters accounted for CAMs (clusters 1, 3, 4, 6, 7, 9, and 13) and four for microglia (clusters 0, 2, 5, and 10). In addition, we detected two clusters for monocytes (clusters 8 and 11)

**Figure 1. Identification of myeloid cell transcriptional clusters in brains of SPF and GF mice by scRNA-seq.**

- UMAP representation of 2,745 individual cells from all CNS compartments derived from 2-month-old SPF (green dots) and GF (yellow dots) mice analyzed with scRNA-seq. Each dot represents an individual cell.
- UMAP plots depicting the cumulative expression levels of previously published core signature genes for microglia, CAMs, monocytes, and cDC2. CAMs, CNS-associated macrophages; DC, dendritic cell. The scale bars represent color-coded sequencing depth-corrected log-transformed transcript counts.
- UMAP plots color-coded for the compartment that cells were isolated from. Parenchyma (dark orange); choroid plexus (dark cyan); perivascular space (pink); leptomeninges (violet).
- UMAP plot color-coded for the Seurat clustering results. The cell types were assigned based on the expression of signature genes from panel (B). CAMs, CNS-associated macrophages; DC, dendritic cell.
- Heatmap of the top 10 differentially expressed genes per cluster (adjusted *P*-value of < 0.05 based on Wilcoxon rank-sum tests). The scale bar represents color-coded Pearson residuals.
- Stacked bar plot (Marimekko chart) color-coded for the relative contribution of cells derived from the respective anatomical regions. Ranges of *P*-values are provided for significantly enriched regions per cluster, based on hypergeometric tests. Benjamini–Hochberg correction was applied to correct for multiple testing (\**P* < 0.05; \*\**P* < 0.01; \*\*\**P* < 0.001).
- Stacked bar plot (Marimekko chart) color-coded for the relative contribution of cells derived from SPF (green) and GF (yellow) mice. Ranges of *P*-values are provided for significantly enriched condition per cluster, based on hypergeometric tests. Benjamini–Hochberg correction was applied to correct for multiple testing (\**P* < 0.05; \*\**P* < 0.01; \*\*\**P* < 0.001).
- UMAP maps color-coded for transcript counts of genes enriched in subsets of the analyzed cells. The scale bars represent color-coded sequencing depth-corrected log-transformed transcript counts.



and one for DCs (cluster 12), lymphocytes (cluster 16), stromal (cluster 15), and proliferating cells (cluster 14), respectively (Fig 1D). Heatmap representation of top 10 differentially expressed genes (DEG) per cluster highlighted differences across the transcriptional spectrum of CNS macrophages (Fig 1E, Dataset EV1 for cluster marker genes). Most clusters showed a predominant relative contribution of cells derived from certain anatomical regions (Fig 1F, Dataset EV2 for hypergeometric test statistics). Notably, all SPF and GF samples contributed to the 17 clusters, while we identified statistically significant (hypergeometric test, adjusted  $P < 0.05$ ) enrichment of GF-derived cells for the clusters 0, 3, 10, and 11 and on the other hand more cells originating from SPF CNS tissues for the clusters 1, 2, and 8 (Fig 1G, Dataset EV2). Overall, the microglial clusters 0, 2, 5, and 10 were characterized by high expression of microglial core genes, including *P2ry12*, *Tmem119*, *Hexb*, *Cystatin 3* (*Cst3*), and *G protein-coupled receptor 34* (*Gpr34*) (Fig 1D, E, and H). Further, clusters 1, 3, 4, 6, 7, 9, and 13 were attributed to CAMs with elevated expression of typical genes including *Mrc1*, *Cd163*, *Lyve1*, *Platelet factor 4* (*Pf4*), *Membrane-spanning 4-domain subfamily A member 7* (*Ms4a7*), *Stabilin-1* (*Stab1*), and *Carbonyl reductase 2* (*Cbr2*). The monocyte cluster 11 was characterized by the expression of *Ccr2* and *Histocompatibility class II antigen A alpha* (*H2-Aa*) indicating classical Ly6C<sup>hi</sup> monocytes, while monocyte cluster 8 expressed higher levels of *Nuclear receptor subfamily 4 group A member 1* (*Nr4a1*) indicating non-classical Ly6C<sup>lo</sup> monocytes (Mildner et al, 2017) (Fig 1D, E, and H). Clusters 12 and 16 showed expression of DC and lymphocyte genes, such as *Cd209a* and *Natural killer cell granule protein 7* (*Nkg7*), respectively (Fig 1D, E, and H). Cluster 15 was composed of a few mixed stromal cells from the brain parenchyma and border regions. Finally, cluster 14 contained cells expressing genes associated with proliferation, including *Marker of proliferation mki-67* (*Mki67*) (Fig 1D, E, and H). Additionally, subsets of cells in cluster 14 showed expression of microglial and CAM signature genes, such as *Tmem119* and *Mrc1*, suggesting a mix of different cell types in this cluster (Fig 1D, E, and H).

To confirm the expression on protein level, we quantified the proportion of CD206 positively labeled Iba1<sup>+</sup> microglia, cpMΦ, pvMΦ, and mMΦ (Fig EV2). Interestingly, Iba1<sup>+</sup> pvMΦ and mMΦ presented a higher percentage of double labeling with CD206 compared to cpMΦ, while we did not detect CD206<sup>+</sup>Iba1<sup>+</sup> parenchymal microglial cells (Fig EV2A–C). However, we found no alterations of Iba1<sup>+</sup>CD206<sup>+</sup> CAMs in brains from GF mice compared with SPF controls, suggesting that gut microbiota do not impair the expression of the typical marker gene CD206 in CAMs (Fig EV2A–C).

To analyze gradual changes across clusters, we conducted pseudotime analysis of microglia and CAMs using StemID2 (Grun et al, 2016). In an unsupervised manner, the algorithm suggested trajectories connecting the microglial (2 → 0 → 10) and CAM (7 → 1 → 4) clusters (Fig EV3) (Herman et al, 2018). The gene expression profiles underlying these trajectories grouped into modules with similar gene expression patterns, and their z-scores were visualized for each of the two compartments of interest (Fig EV3, Datasets EV3 and EV4 for genes along the microglial and CAM trajectories). Notably, clusters that were enriched for cells from GF mice (i.e., cluster 10 for microglia) showed higher expression levels of *ApoE* while clusters enriched for cells from SPF mice showed higher levels of genes associated with immune function, including *Lymphocyte antigen 86* (*Ly86*, also known as *Md-1*) (Fig EV3, Datasets EV3 and

EV4). These findings suggest that the presence of microbiota drives microglia and CAM polarization toward an immunogenic transcriptional phenotype.

To investigate the functional states of the identified macrophage clusters, we performed gene ontology (GO) enrichment analysis based on cluster-enriched gene sets (Appendix Fig S1, Dataset EV5 for an overview of enriched GO terms). Most microglial and CAM clusters showed enrichment for terms linked to immune function such as *Chemotaxis*, *Phagocytosis*, and *Myeloid cell homeostasis* (Appendix Fig S1). Further, several myeloid cell clusters were characterized by the enrichment of the GO terms *Regulation of response to external stimulus* and *Response to bacterium*. The term *Antigen processing and presentation of peptide antigen* was associated with all CAM clusters except cluster 3 that was mainly assembled by cells from GF brains. Notably, the microglial clusters 0 and 10 that were mainly composed of GF-derived cells showed either no association with this term (cluster 0) or only 5 associated genes (cluster 10) (Appendix Fig S1, Dataset EV5). Furthermore, the term *Cytokine secretion* was not correlated with the two clusters 0 and 10 possibly suggesting attenuated immune priming. Clusters 7, 1, and 13 (attributed to CAMs) showed enrichment of the GO term *Interleukin-1 production* (Appendix Fig S1). The proliferating cell cluster showed enrichment of the term *Regulation of mitotic cell cycle* and *Interferon gamma production* was solely attributed to lymphocytes (cluster 16) (Appendix Fig S1).

These findings suggest that CAMs and microglia are affected by the microbiota composition.

### Microbiota-dependent transcriptional heterogeneity of microglia

To further characterize CNS myeloid cells from SPF- and GF-housed mice, we first analyzed their morphology (Appendix Fig S2). As previously shown (Erny et al, 2015), we observed enlarged microglial cells with significantly increased surface area and volume in the cortex of GF mice compared with SPF-housed mice (Appendix Fig S2A). In contrast, cpMΦ, mMΦ, and pvMΦ exhibited no significant morphological divergences at the respective border regions (Appendix Fig S2B–D).

By using bulk RNA-seq, we determined previously that microglia from GF mice display an altered gene expression signature as compared to microglia from SPF mice (Erny et al, 2015). However, it remained unclear whether the composition and heterogeneity of microglia on a single-cell level is changed. Therefore, we assessed potential compartment-specific signatures of microglia from SPF and GF mice in the subset of CNS parenchyma-derived cells (Fig 2). This revealed 828 individual microglial cells derived from SPF and GF brains with typical marker expression which clustered in one scattered microglia cloud with eight subsets, suggesting a spectrum of gradual transcriptional changes (Fig 2A–C, Table EV2 for cell counts per cluster and condition and Dataset EV6 for cluster marker genes). Microglia from clusters 3, 4, and 7 were predominantly GF-derived, whereas clusters 2 and 6 comprised significantly more SPF-derived cells (Fig 2D, Dataset EV7 for hypergeometric test statistics). Analysis of SPF and GF microglia showed several DEG including marked higher abundance of *Ly86*, a marker linked to cell activation (Jordao et al, 2019) and *Cd180* which forms a cell surface receptor complex with *Ly86* (Nagai et al, 2002) for SPF microglia. Concomitant GF microglia featured higher expression of *Complement C1q B chain* (*C1qb*) and *DNA-damage-inducible transcript 4* (*Ddit4*)

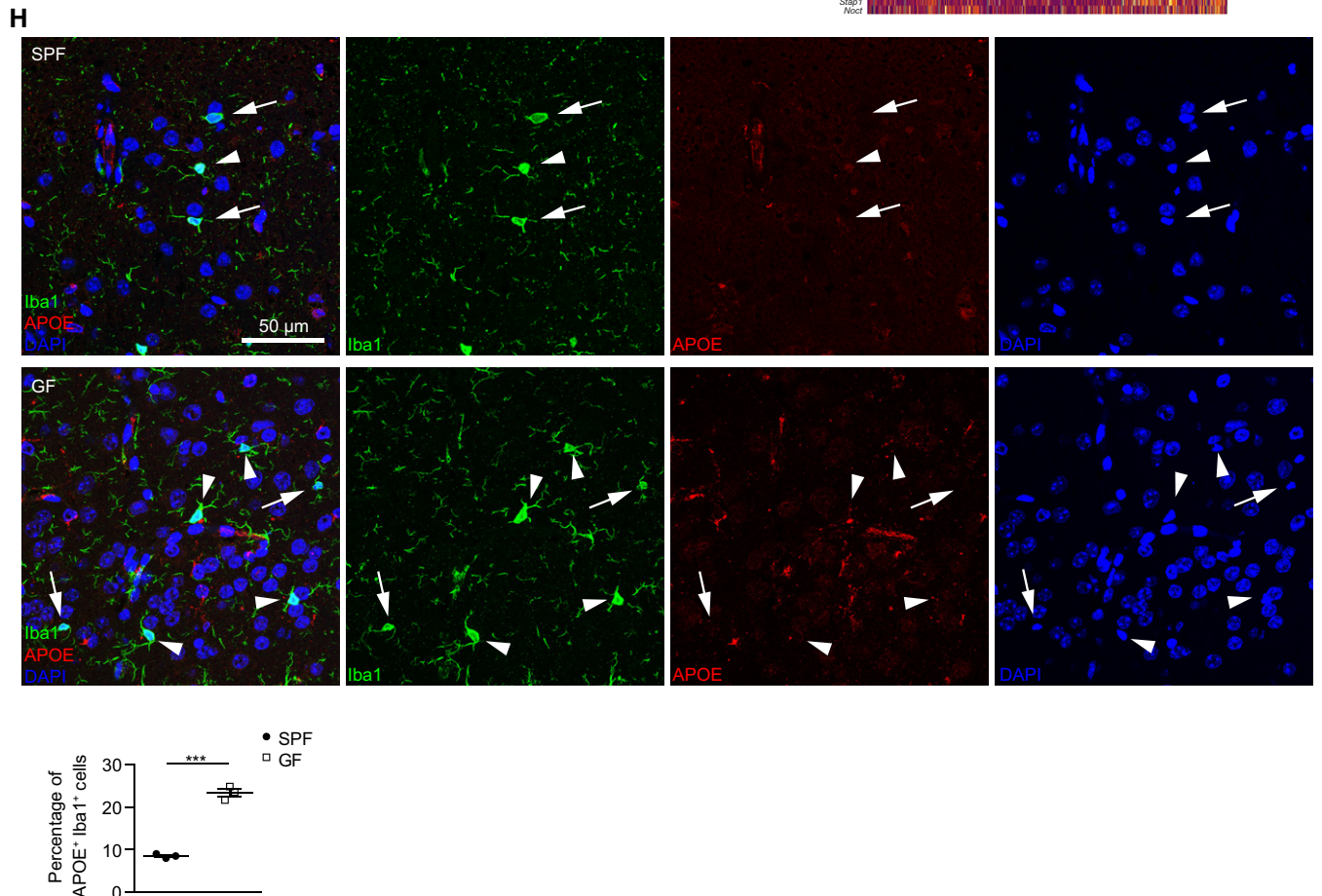
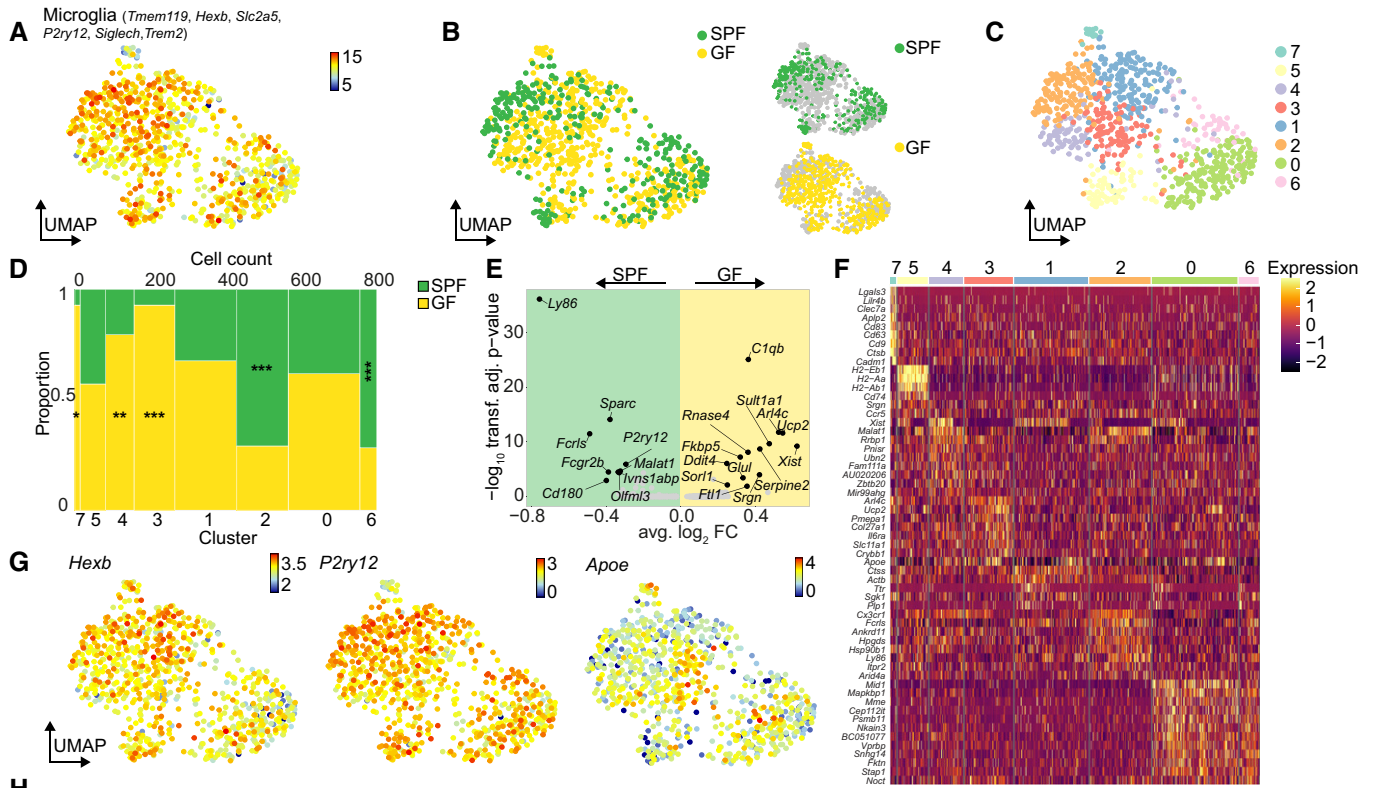


Figure 2.

**Figure 2. Microbiota-dependent alterations in the microglial genetic profile.**

- A UMAP plot illustrating the color-coded aggregate transcript counts of published core signature genes for microglia. The scale bar represents color-coded sequencing depth-corrected log-transformed transcript counts.
- B UMAP representation of 828 individual microglial cells from brain parenchyma derived from SPF (green dots) and GF (yellow dots).
- C UMAP representation of microglial cells of SPF and GF mice color-coded for the results of Seurat clustering. The legend on the right-hand side of the plot shows the color cluster mapping.
- D Stacked bar plot (Marimekko chart) color-coded for the relative clusterwise contribution of microglial cells derived from SPF (green) and GF (yellow) mice. Ranges of *P*-values are provided for significantly enriched regions per cluster, based on hypergeometric tests. Benjamini–Hochberg correction was applied to correct for multiple testing (\**P* < 0.05; \*\**P* < 0.01; \*\*\**P* < 0.001).
- E Volcano plot of the differential gene expression analysis of *n* = 318 SPF and 510 GF cells based on Wilcoxon rank-sum tests. The shown genes are filtered based on an average log<sub>2</sub> fold change (avg. log<sub>2</sub>FC) > 0.2 and adjusted *P*-value < 0.05.
- F Heatmap of the top 10 differentially expressed genes per cluster (adjusted *P*-value of < 0.05 based on Wilcoxon rank-sum tests). The scale bar represents color-coded Pearson residuals.
- G UMAP maps color-coded for transcript counts of genes enriched in subsets of microglial cells. The scale bars represent color-coded sequencing depth-corrected log-transformed transcript counts.
- H Representative immunofluorescence images of Iba1 (green) and APOE (red) on cortical sections from SPF and GF mice. Nuclei were stained with DAPI (blue). Scale bar: 50 μm. White arrowheads indicate APOE<sup>+</sup>/Iba1<sup>+</sup> microglia, and arrows show APOE<sup>-</sup>/Iba1<sup>+</sup> microglia. Quantification of APOE<sup>+</sup>/Iba1<sup>+</sup> microglia. Each symbol represents one mouse. At least three slides were examined per individual mouse. Data are presented as mean ± s.e.m. Significant differences were determined by unpaired *t*-test and marked with asterisks (\**P* < 0.05). Data are representative of two independent experiments.

(Fig 2E, Dataset EV8 for overview of all DEGs for this comparison). Previously, *Ddit4* was found to be significantly increased in microglia from GF mice compared with SPF controls based on bulk RNA-seq (Erny *et al*, 2015). We investigated all eight clusters and found, despite dropout rates with undetectable *Ddit4* in a number of cells, elevated *Ddit4* transcript counts for microglial cells from GF mice in all clusters except cluster 7 (Appendix Fig S3). This suggested a mostly consistent *Ddit4* expression across the GF microglial population. While *Hexb* was homogeneously expressed by both SPF and GF microglia, we found higher *ApoE* mRNA levels in microglia from GF animals and verified increased Iba1<sup>+</sup>APOE<sup>+</sup> microglial proportions in GF mice (Fig 2F–H and Appendix Fig S3). Microglial expression of *ApoE* is known to be downregulated during development and might indicate an immature status of GF microglial cells (Butovsky *et al*, 2014). In addition, we detected less *P2ry12* expression in GF microglia and verified reduced percentage of P2RY12<sup>hi</sup>Iba1<sup>+</sup> cells in the cortex of GF mice compared with SPF controls (Figs 2E and G, and EV2D–F and Appendix Fig S3).

By re-evaluating microglial densities through Iba1 immunohistochemistry, we observed increased microglial numbers in the cortex of GF mice compared with age- and sex-matched SPF controls (Fig EV4A and B). Postnatal antibiotic treatment (ABX) for 4 weeks did not affect microglial density. A highly limited gut bacteria diversity as displayed in tri-colonized ASF mice (Stecher *et al*, 2010) or stable defined moderately diverse mouse microbiota (sDMDMm2) mice with 12 selected bacterial strains (Uchimura *et al*, 2016) revealed microglial numbers comparable to GF mice that were in turn restored upon colonization by SPF donors with diverse gut bacteria composition (Fig EV4A and C–E). While microbiota-associated molecular pattern (MAMP) recognized by TLR2, TLR3, TLR4, TLR7, and TLR9 that all use either MyD88- or TRIF-dependent signaling (Kawai & Akira, 2009) were not involved in the maintenance of microglia under homeostatic conditions, instead, we found that a mixture of bacterial derived short-chain fatty acids (SCFAs), namely acetate, butyrate, and propionate, enabled recovery of microglial numbers, while the precise molecular mechanism remained unsolved (Erny *et al*, 2015) (Fig EV4A, F, and G). Further, the absence of the free fatty acid receptor 2 (FFAR2) that can bind SCFAs did not result in altered microglial numbers (Fig EV4A and H).

In sum, these findings showed that the overall composition and heterogeneity of microglia harbors specific microbiota-dependent alterations while microglial density is highly plastic and can be modulated by complex microbiota and is mediated by the microbiota-derived metabolite SCFAs.

### Complex microbiota controls choroid plexus macrophage properties

Next, we profiled the CAM populations from the choroid plexus separately, whereby 487 single cells from healthy SPF and GF mice resulted in eight subsets with statistically significant enrichment of SPF-derived cells in cluster 5, while cluster 1 was predominantly composed of GF-derived cells (Fig 3A–D, Table EV3 for cluster cell counts per condition, Dataset EV9 for cluster marker genes and Dataset EV10 for hypergeometric test statistics). We observed two transcriptionally distinct CAM subsets corresponding to cpMΦ (clusters 0, 1, and 5) and Kolmer epiplexus (CP<sub>epi</sub>) cells (clusters 2–4) (Fig 3C). While cpMΦ expressed typical CAM signature genes (Fig 1A left), CP<sub>epi</sub> cells displayed expression of genes usually attributed as typical microglial markers (Van Hove *et al*, 2019) (Fig 1A right). Differential gene expression analysis between SPF and GF cpMΦ showed higher expression of *Ly86* in SPF and *ApoE* in GF cpMΦ, respectively (Fig 3E, Dataset EV11 for overview of all DEGs for this comparison). Additionally, DEG of SPF CP<sub>epi</sub> cells included *Cd52* and *Guanine nucleotide binding protein, alpha stimulating* (*Gnas*) while GF CP<sub>epi</sub> cells showed higher expression of *ApoE* and *Abca1*, suggesting that GF cpMΦ and CP<sub>epi</sub> cells might mirror a rather immature state analogous to GF microglia (Figs 3E and EV5A). Overall, *Cst3*, *Sparc*, *P2ry12*, and *Hexb* showed higher abundance in clusters 2–4 attributed to CP<sub>epi</sub> cells, *ApoE*, *Mrc1*, and *Stab1* in clusters 0 and 1 referring to cpMΦ (Fig 3F and G, Dataset EV9). P2RY12 positively labeled Iba1<sup>+</sup> CAMs were identifiable in the choroid plexus by immunohistochemistry, whereby we found no differences due to the GF status (Fig EV2D–F). In addition, we noticed significantly more APOE<sup>+</sup>Iba1<sup>+</sup> CAMs in the choroid plexus of GF mice compared with SPF controls supporting the scRNA-seq data (Fig EV2G–I). Besides, the dataset contained some proliferating (cluster 7) and stromal cells (cluster 6) and showed expression of,

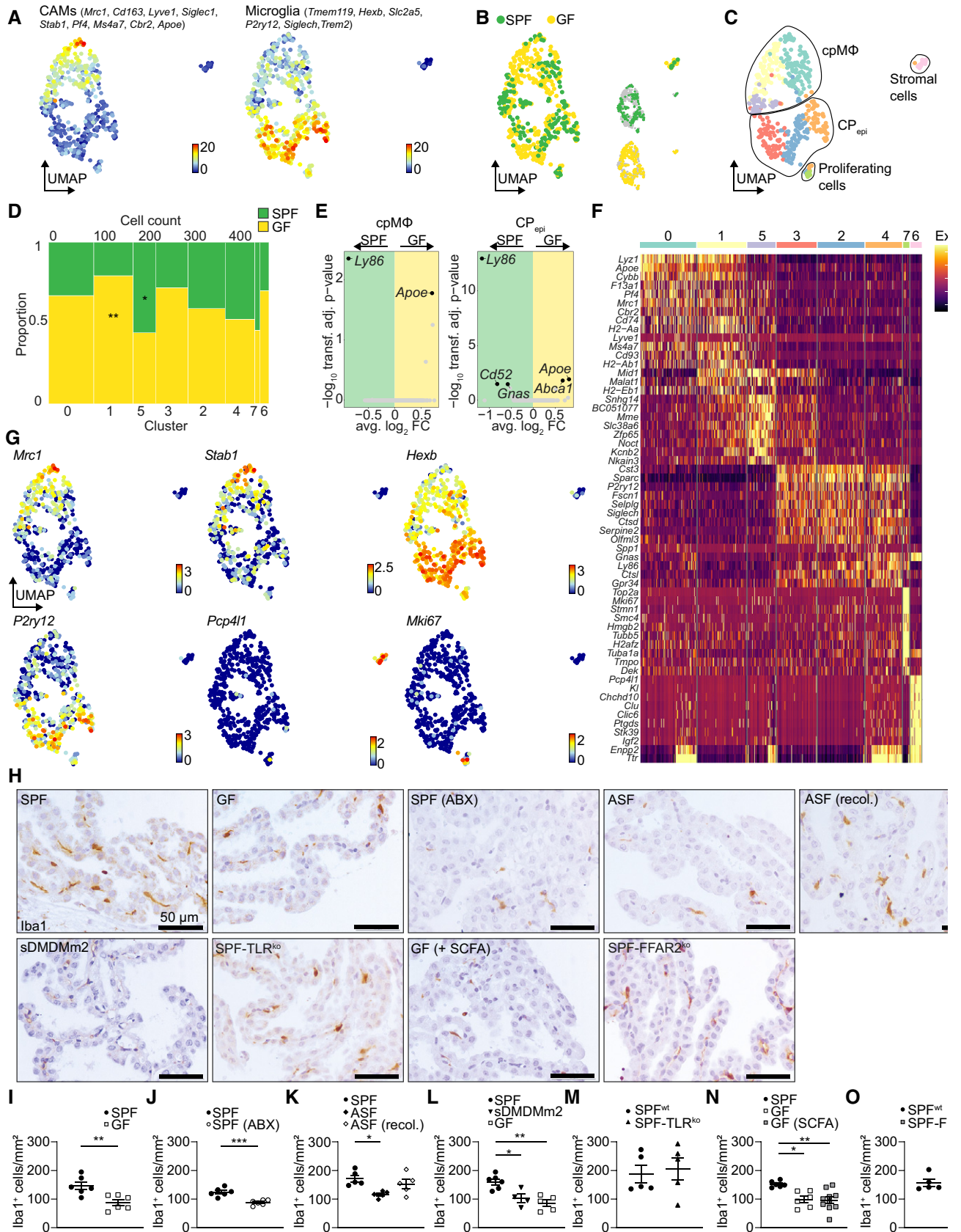


Figure 3.

**Figure 3. Choroid plexus macrophage properties are controlled by complex microbiota.**

- A UMAP plot illustrating the color-coded aggregated transcript counts of published core signature genes for CAMs and microglia. The scale bars represent color-coded sequencing depth-corrected log-transformed transcript counts.
- B UMAP representation of 487 individual choroid plexus cells from lateral and fourth ventricles of SPF (green dots) and GF (yellow dots) mice.
- C UMAP representation of the choroid plexus cells of SPF and GF mice color-coded for the Seurat cluster assignment. The color cluster mappings are indicated on the right-hand side of the plot. The cell type annotations are based on published gene expression profiles.
- D Stacked bar plot (Marimekko chart) presenting the color-coded relative contribution of choroid plexus cells derived from SPF (green) and GF (yellow) mice. Ranges of *P*-values are provided for significantly enriched regions per cluster, based on hypergeometric tests. Benjamini–Hochberg correction was applied to correct for multiple testing (\**P* < 0.05; \*\**P* < 0.01).
- E Volcano plots of the differential gene expression analysis of *n* = 51 SPF and 136 GF stromal cpMΦs (left) and *n* = 85 SPF and 134 GF Kolmer epiplexus cell (CP<sub>epi</sub>) cells (right) based on Wilcoxon rank-sum tests. The shown genes are filtered based on an avg. log<sub>2</sub>FC > 0.2 and adjusted *P*-value < 0.05.
- F Heatmap of the top 10 differentially expressed genes per cluster (adjusted *P*-value of < 0.05 based on Wilcoxon rank-sum tests). The scale bar represents color-coded Pearson residuals.
- G UMAP maps color-coded for transcript counts of genes enriched in subsets of choroid plexus cells. The scale bars represent color-coded sequencing depth-corrected log-transformed transcript counts.
- H Representative Iba1<sup>+</sup> immunohistochemistry in the choroid plexus of SPF, GF, ABX-treated, ASF, recolonized ASF, sDMDMm2, TLR2-, TLR3-, TLR4-, TLR7-, TLR9-deficient, SCFA-treated GF mice or FFAR2-deficient mice. Scale bar = 50 μm.
- I–O Quantification of stromal CPMΦ. Each symbol represents one mouse. Three to four sections per mouse were examined. Means ± s.e.m. are indicated. Significant differences were evaluated by unpaired *t*-test or one-way ANOVA followed by Tukey's *post hoc* comparison test and marked with asterisks (\**P* < 0.05, \*\**P* < 0.01, \*\*\**P* < 0.001). Data are representative of at least two independent experiments.

e.g., *Purkinje cell protein 4-like 1* (*Pcp4l1*), *Clusterin* (*Clu*) and *Mki67*, respectively (Fig 3F–G, Dataset EV9).

Next, we quantified Iba1<sup>+</sup> CAMs in the choroid plexuses of lateral and fourth ventricles of SPF and GF animals and found a marked reduction of stromal cpMΦ in GF mice (Fig 3H and I), which is in contrast to increased numbers of parenchymal microglia in these animals (Fig EV4A and B). Remarkably, the density of CP<sub>epi</sub> was not affected by gut bacteria (Fig EV5B and C). Further, upon treatment with ABX, the number of stromal cpMΦ significantly declined (Fig 3H and J), which is again in contrast to stable microglial numbers (Fig EV4A and C) indicating that CNS myeloid cells are divergently regulated by gut microbiota. While a highly limited composition of gut bacteria—as reflected in both ASF and sDMDMm2 mice—caused a significant reduction of stromal cpMΦ numbers (Fig 3H, K, and L), mice recolonized with complex gut microbiota from SPF donors showed restored stromal cpMΦ densities as observed in SPF animals (Fig 3H and K). Next, we investigated whether distinct MAMPs influence stromal cpMΦ densities. However, TLR2-, TLR3-, TLR4-, TLR7-, and TLR9-deficient mice did not manifest altered stromal cpMΦ numbers (Fig 3H and M). Surprisingly, treatment with SCFAs failed to restore stromal cpMΦ quantities (Fig 3H and N), which contrasts with their counterparts in the CNS parenchyma, the microglia (Fig EV4A and G). Additionally, FFAR2 deficiency did not affect stromal cpMΦ density (Fig 3H and O), indicating a dispensable role of SCFAs/FFAR2 signaling for stromal cpMΦ.

Overall, these findings support the presence of distinct CAM subpopulations in the choroid plexus that are divergently shaped by microbiota with a high diversity while the signaling from the gut to the choroid plexus seemed to be independent of SCFA.

**Single-cell analysis of perivascular macrophages in GF mice**

Subsequently, we investigated 885 cells derived from the perivascular space from SPF- and GF-housed mice (Fig 4A and B, Table EV4 for cluster cell counts per condition). We observed five subsets (clusters 0, 1, 2, 6, and 9) of pvMΦ with enrichment of SPF cells in cluster 2 and GF cells in cluster 6 (Fig 4C and D, Dataset EV12 for cluster marker genes and Dataset EV13 for hypergeometric test

statistics). Furthermore, few microglia, cDCs, lymphocytes, and Ly6C<sup>lo</sup> and Ly6C<sup>hi</sup> monocytes and were captured (Fig 4C). DEG analysis of pvMΦ from SPF and GF animals showed higher expression levels of *Ly86* and *Fc receptor-like 5*, *scavenger receptor* (*Fcrl5*) in SPF cells and *Cd163*, *Lyve1*, and *Cd209b* in GF pvMΦ (Fig 4E, Appendix Fig S4, Dataset EV14 for overview of all DEGs for this comparison). Higher *ApoE* mRNA levels were detected in cluster 6 that was mainly composed of GF-derived cells (Dataset EV12). Increased proportion of APOE<sup>+</sup>Iba1<sup>+</sup> cells in the perivascular space was confirmed by immunohistochemistry (Fig EV2G–I). PvMΦ expressed typical markers for CAMs such as *Mrc1*, *Cd163*, *Pf4*, *Stab1*, and *Cbr2* (Fig 4F and G), whereas *Ctsc* gene transcripts presented heterogeneous expression patterns with higher abundance of *Ctsc* transcripts in cluster 0 (Fig 4F, Dataset EV14). Clusters 3 and 4 were mainly composed of Ly6C<sup>hi</sup> or Ly6C<sup>lo</sup> monocytes, respectively, and showed relatively increased transcripts for *Ccr2* or *Nr4a1* (Fig 4C, F, and G). Microglia (cluster 7) presented higher *Hexb* expression and lymphocytes (cluster 8) were characterized by higher numbers of *Nkg7* mRNA transcripts (Fig 4C, F, and G).

Furthermore, we explored pvMΦ in the perivascular space of cortical areas by Iba1 immunohistochemistry in SPF and GF mice (Fig 4H and I). However, we discerned no shifts for pvMΦ numbers in mice lacking microorganisms, as well as by microbiota eradication through ABX treatment, in mice with limited gut bacteria composition, after recolonization with diverse composed microbiota, SCFAs application, and in mice lacking TLR2, TLR3, TLR4, TLR7, TLR9, or FFAR2 deficiency (Fig 4H–O), indicating that pvMΦ quantities are not affected through constitutive (GF), induced (ABX) gut microbiota depletion or limited complexity (ASF, sDMDMm2) at steady-state conditions.

In sum, these findings suggest that the transcriptional profile of pvMΦ is controlled by intestinal microbiota whereas cell numbers remain stable.

**The transcriptional profile of meningeal macrophages under GF conditions**

Next, we analyzed the transcriptional profiles of 545 leptomeningeal cells from mice housed under SPF and GF conditions, respectively.



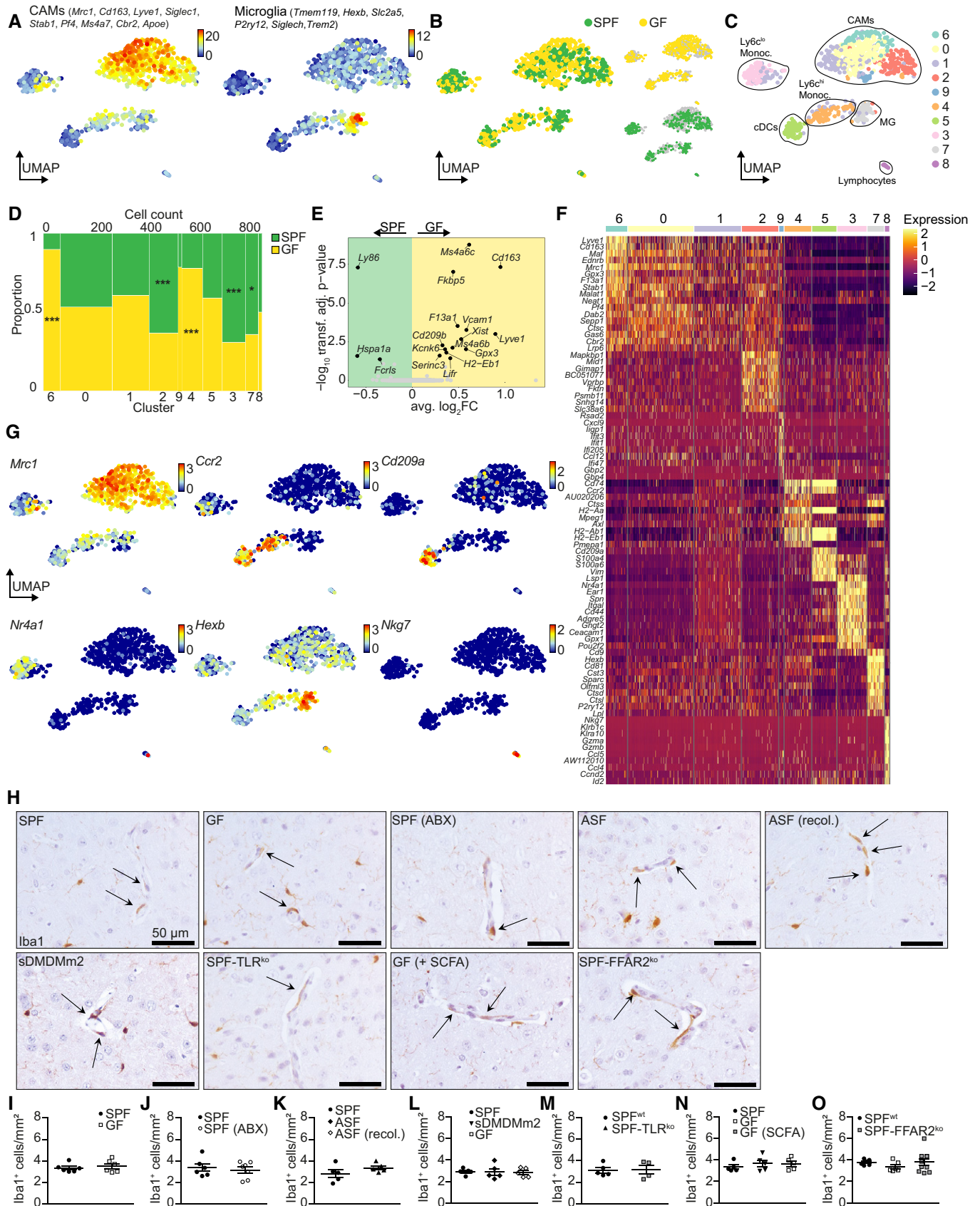


Figure 4.

**Figure 4. Perivascular macrophages show microbiota-dependent transcriptional alterations under steady-state conditions.**

- A UMAP plot illustrating the color-coded aggregated transcript counts of published core signature genes for CAMs. The scale bar represents color-coded sequencing depth-corrected log-transformed transcript counts.
- B UMAP representation of 885 individual cells from SPF (green dots) and GF (yellow dots) mice.
- C UMAP plot of the perivascular macrophages from SPF and GF mice color-coded for the results of Seurat clustering. The mappings between colors and clusters are shown on the right. The cell type annotations are based on published gene expression profiles.
- D Stacked bar plot (Marimekko chart) color-coded for the relative contribution of perivascular macrophages derived from SPF (green) and GF (yellow) mice. *P*-value ranges are provided for significantly enriched regions per cluster, based on hypergeometric tests. Benjamini–Hochberg correction was applied to correct for multiple testing (\**P* < 0.05; \*\*\**P* < 0.001).
- E Volcano plot of the differential gene expression analysis of *n* = 182 SPF and 228 GF pvMΦ based on Wilcoxon rank-sum tests. The shown genes are filtered based on an average log<sub>2</sub> fold change (avg. log<sub>2</sub>FC) > 0.2 and adjusted *P*-value < 0.05.
- F Heatmap of the top 10 differentially expressed genes per cluster (adjusted *P*-value of < 0.05 based on Wilcoxon rank-sum tests). The scale bar represents color-coded Pearson residuals.
- G UMAP maps color-coded for transcript counts of genes enriched in subsets of the captured cells. The scale bars represent color-coded sequencing depth-corrected log-transformed transcript counts.
- H Representative Iba1<sup>+</sup> immunohistochemistry in the perivascular space of SPF, GF, ABX-treated, ASF, recolonized ASF, sDMDMm2, TLR2-, TLR3-, TLR4-, TLR7-, TLR9-deficient, SCFA-treated GF mice or FFAR2-deficient mice. Arrows indicate Iba1<sup>+</sup> perivascular macrophages. Scale bar = 50 μm.
- I–O Quantification thereof. Each symbol represents one mouse. Three to four sections per mouse were examined. Means ± s.e.m. are indicated. No significant differences were determined by unpaired *t*-test or one-way ANOVA followed by Tukey's *post hoc* comparison test. Data are representative of at least two independent experiments.

We found three subsets of mMΦ (clusters 0, 2, and 7) with significantly increased numbers of SPF-derived macrophages in clusters 0 and 2 (Fig 5A–D, Table EV5 for cluster cell counts per condition, Dataset EV15 for cluster marker genes and Dataset EV16 for hypergeometric test statistics). Besides mMΦ, microglia (clusters 1, 3, 5, 6, and 8), Ly6c<sup>lo</sup> (cluster 9) and Ly6c<sup>hi</sup> monocytes, and cDCs (both in cluster 4) were captured (Fig 5C). In contrast to cpMΦ, pvMΦ, and microglia, DEG analysis showed no major differences between SPF and GF mMΦ except higher expression of *Chondroitin sulfate proteoglycan 5* (*Cspg5*) in GF mMΦ (Fig 5E). Overall, mMΦ expressed *Mrc1*, *Cd163*, *Pf4*, *Stab1*, and *Cbr2* (Fig 5F and G). The percentage of APOE<sup>+</sup>Iba1<sup>+</sup> meningeal cells was not affected by the GF status (Fig EV2G–I). *Nr4a1* was mainly expressed in Ly6c<sup>lo</sup> monocytes, *Ccr2* in Ly6c<sup>hi</sup> monocytes and alongside with *Cd209a* in cDCs (Fig 5F and G). *Hexb* and *P2ry12* were mainly expressed by microglia with a reduced expression of the latter gene in clusters 6 and 8 that were mainly composed by GF-derived microglia (Fig 5F and G).

To determine whether the gut microbiota is essential for the mMΦ numbers, we examined Iba1<sup>+</sup> mMΦ in the leptomeninges by immunohistochemistry (Fig 5H). Overall, we noticed no alterations for Iba1<sup>+</sup> mMΦ in mice lacking microorganisms or by different microbiota manipulation strategies, namely through recolonization, SCFA supplementation, TLR2, TLR3, TLR4, TLR7, TLR9, and FFAR2 deficiency (Fig 5H–O), indicating that gut microbiota does not affect mMΦ numbers.

Collectively, these results suggested minor influences of gut bacteria on mMΦ.

#### Microbiota-dependent innate immune response of CNS myeloid subsets to acute cerebral LCMV infection

Macrophages are the first responders to infections of the brain, mediating early pathogen control and initiating downstream immune reactions (Prinz *et al*, 2017; Kierdorf *et al*, 2019). To examine the functional consequences of CNS macrophage alterations in

**Figure 5. Meningeal macrophages display subtle changes through the absence of the microbiota under steady-state conditions.**

- A UMAP plot illustrating the color-coded aggregated transcript counts of published core signature genes for CAMs. The scale bar represents color-coded sequencing depth-corrected log-transformed transcript counts.
- B UMAP representation of 545 individual cells of SPF (green dots) and GF (yellow dots) mice.
- C UMAP representation of the meningeal macrophages of SPF and GF mice color-coded for the clustering results of the Seurat algorithm. The mappings between colors and clusters are shown on the right. The cell type annotations are based on published gene expression profiles.
- D Stacked bar plot (Marimekko chart) color-coded for relative contribution of meningeal macrophages derived from SPF (green) and GF (yellow) mice. *P*-value ranges are provided for significantly enriched regions per cluster, based on hypergeometric tests. Benjamini–Hochberg correction was applied to correct for multiple testing (\**P* < 0.05; \*\*\**P* < 0.001).
- E Volcano plot of the differential gene expression analysis of *n* = 132 SPF and 81 GF mMΦs based on Wilcoxon rank-sum tests. The shown genes are filtered based on an average log<sub>2</sub> fold change (avg. log<sub>2</sub>FC) > 0.2 and adjusted *P*-value < 0.05.
- F Heatmap of the top 10 differentially expressed genes per cluster (adjusted *P*-value of < 0.05 based on Wilcoxon rank-sum tests). The scale bar represents color-coded Pearson residuals.
- G UMAP maps color-coded for transcript counts of genes enriched in subsets of the captured cells. The scale bars represent color-coded sequencing depth-corrected log-transformed transcript counts.
- H Representative Iba1<sup>+</sup> immunohistochemistry in the leptomeninges of SPF, GF, ABX-treated, ASF, recolonized ASF, sDMDMm2, TLR2-, TLR3-, TLR4-, TLR7-, TLR9-deficient, SCFA-treated GF mice, or FFAR2-deficient mice. Arrows indicate Iba1<sup>+</sup> meningeal macrophages. Scale bar = 50 μm.
- I–O Quantification thereof. Each symbol represents one mouse. Three to four sections per mouse were examined. Means ± s.e.m. are indicated. No significant differences were determined by unpaired *t*-test or one-way ANOVA followed by Tukey's *post hoc* comparison test. Data are representative of at least two independent experiments.

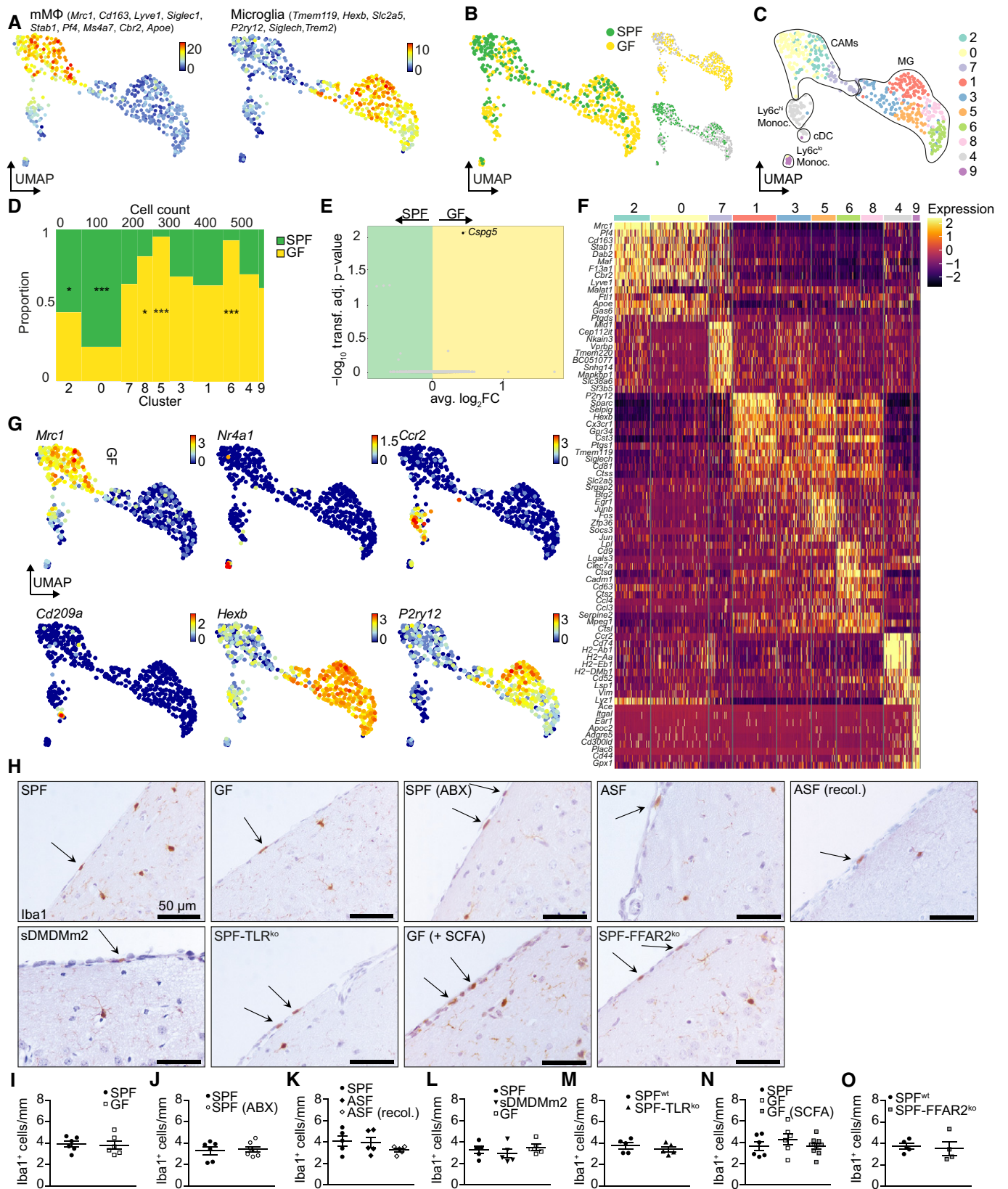


Figure 5.

mice lacking microbes, we infected the animals with LCMV intracerebrally (i.c.) and analyzed CNS myeloid cell expansion after 4 days (Fig 6A and B). Microglia from SPF mice reacted with a strong increase of cell density, whereas the virus-induced microgliosis was less prominent in GF mice. A similar response with elevated Iba1<sup>+</sup> cells numbers was present in the choroid plexus, the leptomeninges, and the perivascular space from mice with gut microbiota while mice devoid of microorganisms presented diminished cell expansion (Fig 6A and B).

Accordingly, the number of proliferating Iba1<sup>+</sup>Ki67<sup>+</sup> microglia and to a lesser degree CAMs was increased under SPF conditions (Fig 6C). To gain further insights about the activation state of the CAMs in LCMV infected brains, we quantified the proportion of CD74<sup>+</sup>Iba1<sup>+</sup> CNS macrophages (Fig 6D). Recently, CD74 was reported as a marker for activated CAMs (Jordao *et al*, 2019). Notably, we found increased CD74<sup>+</sup>Iba1<sup>+</sup> microglial and CAM numbers in all compartments in SPF-housed mice challenged with LCMV compared to PBS controls (Fig 6D). In contrast, in LCMV challenged GF mice the numbers of CD74<sup>+</sup>Iba1<sup>+</sup> remained largely unaffected.

In sum, these data suggest that in GF mice that are devoid of intestinal microorganisms, the innate immune response of CAMs against an acute challenge by an RNA virus is impaired.

#### Perivascular macrophages in AD transgenic mice clear A $\beta$ in a microbiota-dependent manner

To gain further insights into the functional consequences of microbiota-dependent properties of CAMs, we assessed the role of CAMs in a more chronic disease state. To this end, we took advantage of the 5xFAD mouse model of Alzheimer's disease (AD) and observed A $\beta$  depositions in the leptomeninges of the cortex, choroid plexus, hippocampal brain parenchyma, and perivascular space of 4-month-old male SPF, GF, and ABX-treated 5xFAD mice (Fig 7A–C). Recently, we determined that the extent of the A $\beta$  burden in hippocampal regions is gut microbiota-dependent (Mezo *et al*, 2020). Accordingly, we observed reduced A $\beta$  depositions in the hippocampi of the GF and ABX-treated 5xFAD mice (Fig 7C and D). Notably, we found significantly increased cell densities of mM $\Phi$ , cpM $\Phi$ , and pvM $\Phi$  in the respective anatomical regions of SPF 5xFAD mice compared with GF and ABX-treated 5xFAD mice and matched wild-type (WT) controls (Fig 7E–G). To explore the functional role of CAMs in A $\beta$  pathology, we determined the percentage of CAMs that incorporated A $\beta$  by double immunohistochemistry for Iba1 and A $\beta$  (Fig 7A–C). In contrast to mM $\Phi$  and cpM $\Phi$ , A $\beta$ -

containing Iba1<sup>+</sup> pvM $\Phi$  was significantly more frequent in transgenic 5xFAD mice housed under GF conditions compared with SPF 5xFAD mice (Fig 7H–J). Remarkably, the percentage of Iba1<sup>+</sup>A $\beta$ <sup>+</sup> pvM $\Phi$  was also significantly increased after ABX treatment of 5xFAD mice (Fig 7J) suggesting a high plasticity of this effect. We verified this finding by performing *ex vivo* flow cytometric-based analysis of A $\beta$  uptake using methoxy-X-O4 staining (Mezo *et al*, 2020) and detected significantly increased percentage of methoxy-X-O4<sup>+</sup> pvM $\Phi$  under both GF conditions and upon ABX treatment (Fig 7K).

In sum, our data suggest that host microbiota regulate A $\beta$  uptake only in pvM $\Phi$  in AD transgenic mice and thus may contribute to disease outcome by impaired A $\beta$  clearance.

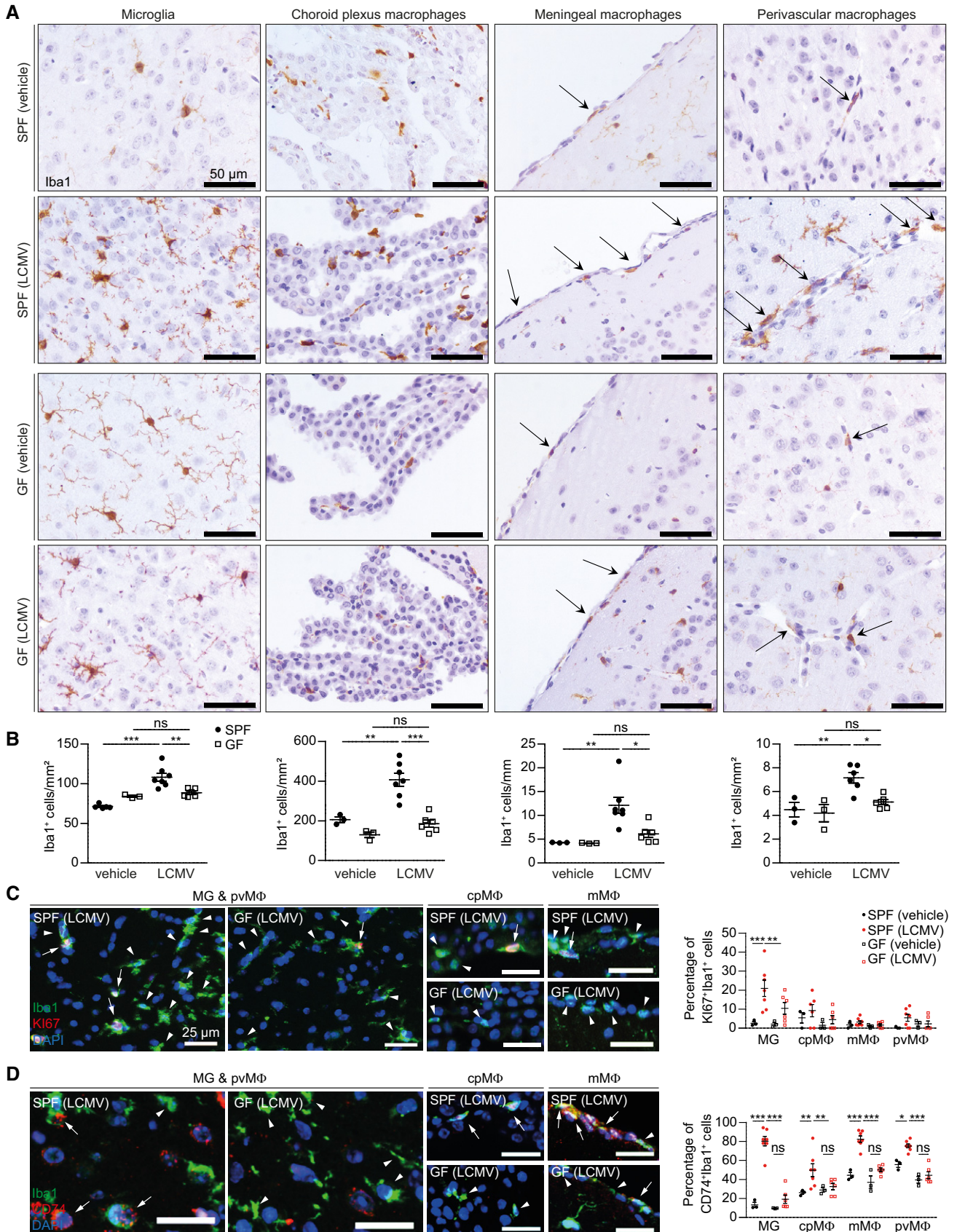
## Discussion

The present study provides a comprehensive analysis of the microbiota-dependent transcriptional landscapes of CNS-resident myeloid subsets. We determined steady-state cell-specific profiles of CNS myeloid cells throughout the various analyzed CNS regions. Previously, we have shown that proper maturation of microglia critically depends on immunological priming by soluble factors produced by a complex microbiota (Erny *et al*, 2015). However, the contribution of gut microbiota on other myeloid cells at CNS interfaces remained unclear. Due to their prominent position at the CNS border regions, CAMs are important immunological gatekeepers of the CNS (Prinz *et al*, 2017; Jordao *et al*, 2019; Kierdorf *et al*, 2019; Brioschi *et al*, 2020). Particularly, the CP has been identified as crucial for the immunological milieu of the brain parenchyma and cerebrospinal fluid with implications for brain development and aging (Baruch *et al*, 2014; Cui *et al*, 2020; Shipley *et al*, 2020).

For microglia, cpM $\Phi$  and pvM $\Phi$ , but not mM $\Phi$  we observed increased expression of *ApoE* in GF mice which was further verified on protein level. Increased *ApoE* expression might be indicative for a rather immature state of the respective macrophage populations. At least for microglia, it is known that *ApoE* is being downregulated during embryonic development (Butovsky *et al*, 2014). Referred to our previous bulk RNA-seq analysis, we detected significantly less DEG in SPF and GF microglia possibly due to the reduced detection/sensitivity of lowly expressed genes in scRNA-seq (Kharchenko *et al*, 2014). As for the cpM $\Phi$  and pvM $\Phi$ , we observed a wider spectrum of transcriptionally distinct clusters compared to mM $\Phi$ , which were largely unaltered. All three CAM subsets featured clusters with elevated expression of typical CAM markers such as *Mrc1*, *Stab1*,

#### Figure 6. Reduced immune response of myeloid cells to LCMV infection under GF conditions.

- A Iba1 immunohistochemistry depicting cortical microglia, meningeal macrophages, perivascular macrophages, and choroid plexus macrophages 4 days after i.c. challenge with LCMV or vehicle controls. Arrows indicate Iba1<sup>+</sup> meningeal or perivascular macrophages, respectively.
- B Quantification of Iba1<sup>+</sup> microglia, choroid plexus macrophages, meningeal macrophages, and perivascular macrophages. Each symbol represents one mouse. Three to four sections per mouse were examined. Significant differences were evaluated by two-way ANOVA followed by Tukey's *post hoc* comparison test and marked with asterisks (\**P* < 0.05, \*\**P* < 0.01, \*\*\**P* < 0.001). Data are representative of two independent experiments.
- C, D Representative immunofluorescence images (left) of (C) Iba1 (green) and Ki67 (red) or (D) CD74 (red) on cortical sections from SPF and GF mice. Nuclei were stained with DAPI (blue). Scale bars: 25  $\mu$ m. White arrows indicate Ki67<sup>+</sup>/Iba1<sup>+</sup> or CD74<sup>+</sup>/Iba1<sup>+</sup> macrophages, and arrowheads show Ki67<sup>-</sup>/Iba1<sup>+</sup> or CD74<sup>-</sup>/Iba1<sup>+</sup> macrophages. Quantification thereof (right). Each symbol represents one mouse. At least three slides were examined per individual mouse. Data are presented as mean  $\pm$  s.e.m. Significant differences were evaluated by two-way ANOVA followed by Tukey's *post hoc* comparison test and marked with asterisks (\**P* < 0.05, \*\**P* < 0.01, \*\*\**P* < 0.001). Data are representative of two independent experiments.



and *Cbr2*. SPF cpMΦ and pvMΦ exhibited increased expression of *Ly86* as microglia did as a sign for cell activation (Jordao et al, 2019). In contrast, CAMs of the choroid plexus additionally had clusters with *P2ry12*-expressing cells. These latter cells likely represent Kolmer epiplexus cells that are transcriptionally distinct from

stromal cpMΦ (Jordao et al, 2019; Van Hove et al, 2019). Both cell populations in the choroid plexus featured microbiota-dependent transcriptional alterations including upregulated *Ly86* and downregulated *ApoE* expression in SPF stromal cpMΦ and CP<sub>epi</sub> compared with GF conditions. Further, only stromal cpMΦ numbers but not

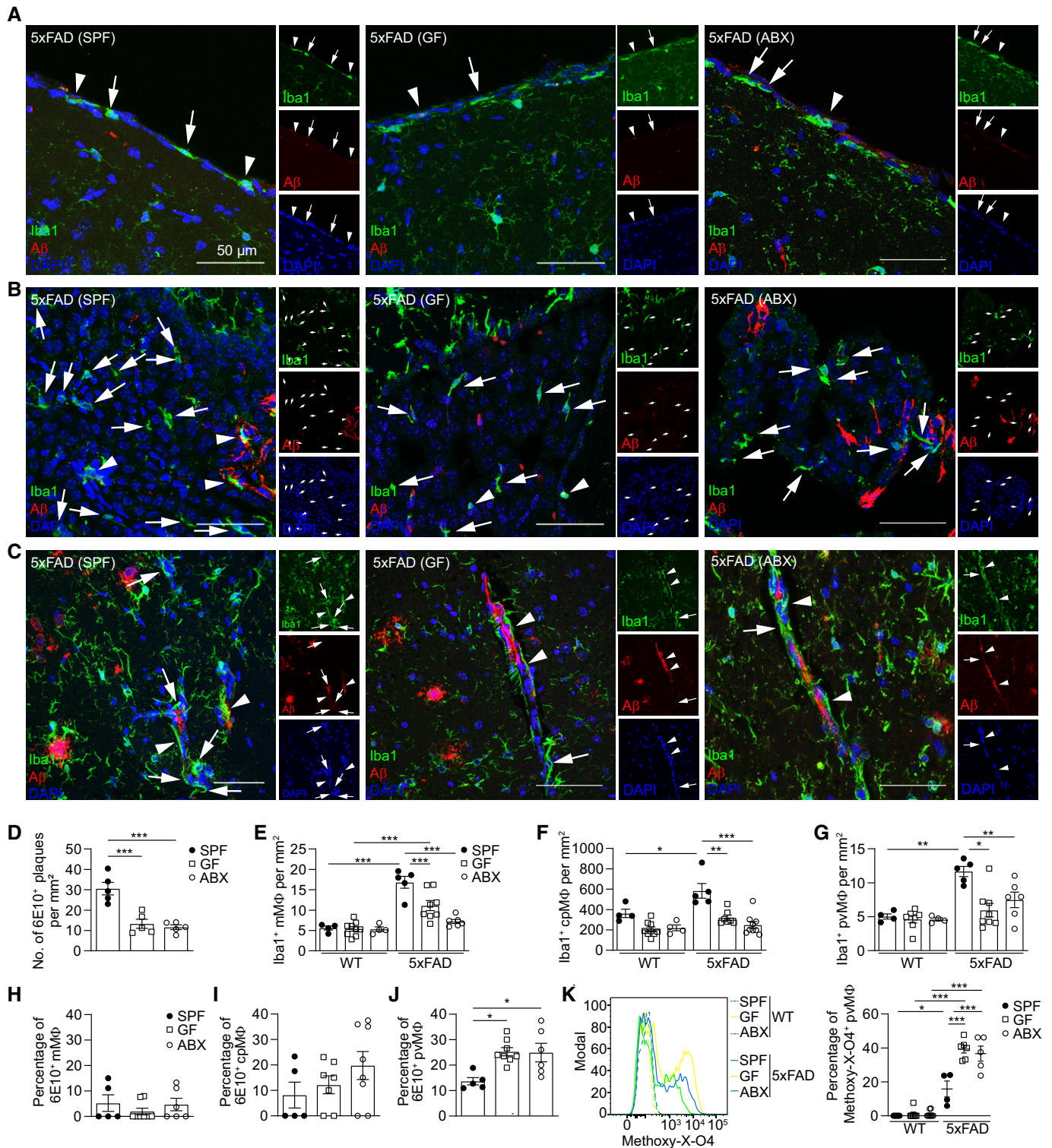


Figure 7.

**Figure 7. Increased A $\beta$  uptake by perivascular macrophages in GF 5xFAD mice.**

- A–C Representative immunofluorescence images visualizing (A) cortical mM $\Phi$ , (B) cpM $\Phi$  located in the lateral ventricle, and (C) hippocampal pvM $\Phi$  from SPF (left), GF (middle), and ABX-treated 5xFAD mice (right). Iba1 (green) and A $\beta$  (6E10, red). Nuclei were stained with DAPI (blue). White arrowheads indicate Iba1<sup>+</sup>A $\beta$ <sup>+</sup> M $\Phi$ , and white arrows show Iba1<sup>+</sup>A $\beta$ <sup>−</sup> M $\Phi$ . Scale bar: 50  $\mu$ m.
- D Quantification of the number of 6E10<sup>+</sup> A $\beta$ -plaques per mm<sup>2</sup>. Each symbol represents one mouse. Means  $\pm$  s.e.m. are indicated. Significant differences were evaluated by one-way ANOVA followed by Tukey's *post hoc* comparison test and marked with asterisks (\*\*\* $P$  < 0.001). Data are representative of four independent experiments.
- E–G Quantification of Iba1<sup>+</sup> (E) mM $\Phi$ , (F) cpM $\Phi$ , and (G) pvM $\Phi$  per mm<sup>2</sup>. Each symbol represents one mouse. At least three slides were examined per individual mouse. Data are presented as mean  $\pm$  s.e.m. Significant differences were determined by two-way ANOVA followed by Tukey's *post hoc* comparison test and marked with asterisks (\* $P$  < 0.05, \*\* $P$  < 0.01, \*\*\* $P$  < 0.001). Data are representative of two independent experiments.
- H–J Percentage of Iba1<sup>+</sup>A $\beta$ <sup>+</sup> (H) cortical mM $\Phi$ , (I) cpM $\Phi$ , and (J) hippocampal pvM $\Phi$  of SPF, GF, and ABX-treated 5xFAD mice. Means  $\pm$  s.e.m. are indicated. Significant differences were evaluated by one-way ANOVA followed by Tukey's *post hoc* comparison test and marked with asterisks (\* $P$  < 0.05). Data are representative of two independent experiments.
- K Representative cytometric graph of methoxy-X-04<sup>+</sup> labeled pvM $\Phi$  from SPF (green line), GF (yellow line), and ABX-treated (blue line) 5xFAD mice and respective WT controls (dashed lines). Quantification of percentages of methoxy-X-04<sup>+</sup> labeled pvM $\Phi$  is depicted. Each symbol represents one mouse. Data are presented as mean  $\pm$  s.e.m. Significant differences were determined by two-way ANOVA followed by Tukey's *post hoc* comparison test (\* $P$  < 0.05, \*\*\* $P$  < 0.001). Data are representative of three independent experiments.

CP<sub>epi</sub> numbers were highly sensitive to different microbiota manipulation strategies which is in line with a previous report, highlighting the critical responsiveness of cpM $\Phi$  to the microbiota (Van Hove *et al*, 2019). In contrast to microglia that presented increased numbers in GF animals (Erny *et al*, 2015), the complete absence of gut commensals in GF-housed mice as well as postnatal depletion of gut bacteria with ABX and a limited gut microbiota composition caused a reduction of stromal cpM $\Phi$ . Conversely, recolonization with complex gut microbiota normalized stromal cpM $\Phi$  numbers indicating that stromal cpM $\Phi$  requires a continuous input from the resident gut bacteria. Gut microbiota-derived MAMPs were shown to mediate steady-state myelopoiesis in the spleen and bone marrow (Khosravi *et al*, 2014). However, we did not observe any alterations in stromal cpM $\Phi$  numbers by analyzing mice with TLR2, TLR3, TLR4, TLR7, and TLR9 deficiency, suggesting other mechanisms than activation of these pattern recognition receptors (PRR) for microbiota-driven effects on stromal cpM $\Phi$ . In contrast to microglia, both SCFAs and the SCFA receptor FFAR2 were redundant for stromal cpM $\Phi$  density under homeostatic conditions, probably due to the dual origin of stromal cpM $\Phi$  (Goldmann *et al*, 2016; Van Hove *et al*, 2019). In contrast to most peripheral tissue macrophages, CAMs and microglia originate from early erythromyeloid yolk sac-derived progenitors during embryonic development (Goldmann *et al*, 2016; Utz *et al*, 2020). It was demonstrated that stromal cpM $\Phi$  is the only CAMs that are replaced by bone marrow-derived cells over time and do not fully self-renew as CP<sub>epi</sub> and their relatives in the meninges, perivascular space, and brain parenchyma (Goldmann *et al*, 2016). Therefore, we speculate that reduced stromal cpM $\Phi$  numbers might be caused by reduced numbers of bone marrow-derived monocytes as it was described in GF mice highlighting potential ontogeny-related cellular differences in CNS macrophages (Khosravi *et al*, 2014; Zhang *et al*, 2015). Interestingly, it was further suggested that diminished monocyte numbers in the bone marrow of GF animals might be caused by decreased levels of growth factors such as CSF1 (Khosravi *et al*, 2014; Zhang *et al*, 2015). Further, reduced monocyte numbers in GF mice could not be normalized through the administration of SCFAs whereby the same SCFA treatment regime was applied as in our analysis (Khosravi *et al*, 2014). Alternatively, it might be possible that levels of local growth factors are altered in the choroid plexus of GF mice and thereby causing decreased numbers of stromal cpM $\Phi$

independent of monocyte-derived cells. Remarkably, mM $\Phi$  and pvM $\Phi$  did not display any changes in their cell densities in GF animals and upon microbiota manipulation with ABX, ASF, sDMDMm2, or SCFA treatments. We speculate that this might be caused through overall relatively low cell numbers of mM $\Phi$  and pvM $\Phi$  in the respective compartments.

Our results further support the idea that a continuous input from complex microbiota is necessary for proper CNS myeloid cell function. Upon acute challenge with LCMV, expansion of CAMs and microglia, as well as the expression of the marker CD74 that is associated with activated CAMs (Jordao *et al*, 2019), was compromised in CAMs of GF mice, indicating that the innate immune response of CNS macrophages is collectively attenuated in the absence of intestinal microbes.

In order to gain further functional insights, we characterized the A $\beta$ -associated pathology using the transgenic 5xFAD mouse model for AD. 5xFAD mice feature A $\beta$  debris around blood vessels, a situation known as cerebral amyloid angiopathy (CAA) (Giannoni *et al*, 2016). Cerebral A $\beta$  levels can be regulated by different A $\beta$  clearance mechanisms, e.g., via the blood–brain barrier (BBB) (Heneka *et al*, 2015), and we therefore asked whether microbiota may influence A $\beta$  clearance by CAMs (Mildner *et al*, 2011). GF 5xFAD mice displayed reduced A $\beta$  pathology, whereby our data suggested for the first time elevated A $\beta$  clearance by pvM $\Phi$  but not mM $\Phi$  or cpM $\Phi$  in GF 5xFAD mice. Previous results indicated ameliorated A $\beta$  levels in GF 5xFAD mice caused by enhanced microglial A $\beta$  uptake (Mezo *et al*, 2020), while A $\beta$  clearance by pvM $\Phi$  might further facilitate removal of A $\beta$ . Notably, the A $\beta$  uptake of microglia was not inducible upon ABX treatment although the A $\beta$  pathology was significantly diminished in these mice (Mezo *et al*, 2020). We speculate that this might be primarily due to augmented A $\beta$  clearance by pvM $\Phi$  upon ABX treatment. Therefore, compromised perivascular clearance of A $\beta$  might be a crucial factor in the accumulation of A $\beta$  in CAA and may be a suitable target for new therapeutic approaches (Hawkes *et al*, 2014). Interestingly, several genes (including *ApoE* and *P2ry12*) that have been recently linked to A $\beta$ -activated microglia in AD mouse models (Keren-Shaul *et al*, 2017; Krasemann *et al*, 2017) displayed elevated expression in microglia and CAMs from GF mice under steady-state conditions, suggesting a possible microbiota-dependent influence on this disease-associated activation state of CNS macrophages. In our previous study, we ruled out the

possibility that processing of the amyloid precursor protein (APP) is altered in the CNS by absent gut bacteria (Mezo *et al*, 2020). Notably, the increased A $\beta$  uptake by microglia and pM $\Phi$  in GF and ABX-treated 5xFAD mice resulted in preserved neuronal density in the hippocampus and related cognitive function (Mezo *et al*, 2020).

In summary, we found that host microbiota is crucial for the properties of selective CNS macrophages at border regions during homeostasis and activation upon acute viral challenge and chronic neurodegeneration. We revealed distinct microbiota-dependent cellular A $\beta$ -clearance mechanisms in the 5xFAD mouse model of AD. These results may further widen our understanding and treatment of CNS macrophage-mediated inflammatory and neurodegenerative diseases of the CNS.

## Materials and Methods

### Mice

Conventional SPF mice on C57BL/6J background were purchased from Janvier labs (Saint-Berthevin, France). Germ-free C57BL/6J mice were obtained from the Clean Mouse Facility (Bern, Switzerland). All mice (mixed sex) were used at 6–10 weeks of age. ASF and recolonized ASF mice on a C57BL/6J (females) were provided by Bärbel Stecher (Max-von-Pettenkofer Institute, LMU Munich, German Center for Infection Research) (Stecher *et al*, 2010). ASF mice colonized with *Bacteroides distasonis* (strain ASF 519), *Lactobacillus salivarius* (strain ASF 361), and Clostridium cluster XIV (ASF 356) were housed under germ-free conditions in a flexible film isolator with HEPA-filtered air and autoclaved chow and bedding. For recolonization, ASF mice were co-housed with conventional SPF donor mice in the same cage for six weeks. Mice with a stable defined moderately diverse mouse microbiota (sDMDMm2) (Uchimura *et al*, 2016), also known as Oligo-MM<sup>12</sup> (Garzetti *et al*, 2017), were obtained from Andrew Macpherson and Mercedes Gomez de Agüero (DBMR, Bern, Switzerland). For substantial depletion of the microbiota, SPF mice were provided with drinking water containing 1 mg/ml cefoxitin (Santa Cruz Biotechnology, Heidelberg, Germany), 1 mg/ml gentamicin (Sigma-Aldrich, Taufkirchen, Germany), 1 mg/ml metronidazole (Sigma-Aldrich, Taufkirchen, Germany), and 1 mg/ml vancomycin (Hexal, Holzkirchen, Germany) for 4 weeks *ad libitum* as described previously (Erny *et al*, 2015). For treatment with short-chain fatty acids, 25 mM sodium propionate, 40 mM sodium butyrate, and 67.5 mM sodium acetate (Sigma-Aldrich, Taufkirchen, Germany) were added to drinking water for four weeks as described previously (Erny *et al*, 2015). Sodium-matched water was provided to control mice. Water solutions were prepared and changed weekly. Ffar2-deficient mice (*Ffar2*<sup>tm1LexFfar2tm1Dgeni</sup>) and wild-type littermate controls (females) were provided by Wendy Garrett (Harvard School of Public Health, Boston, USA). TLR2-, TLR3-, TLR4-, TLR7-, and TLR9-deficient mice (*B6.129-Tlr2<sup>tm1Aki</sup> Tlr3<sup>tm1Aki</sup> Tlr4<sup>tm1Aki</sup> Tlr7<sup>tm1Aki</sup> Tlr9<sup>tm1Aki</sup>*) (Conrad *et al*, 2009) (mixed sex) were provided by Thorsten Buch (University of Zurich, Switzerland).

As a mouse model of Alzheimer's disease, we used heterozygous male 5xFAD (*Tg(APPs<sup>SwFLon</sup>,PSEN1<sup>\*M146L</sup>\*L286V)* 6799Vas) transgenic mice and non-transgenic littermates (4 months

of age) on a C57BL/6J background co-expressing human APP<sup>K670N/M671L</sup> (Sw)+I716V (Fl)+V717I(Lo) and PS1<sup>M146L+L286V</sup> under the control of the neuron-specific Thy-1 promoter (Oakley *et al*, 2006). Mice were housed under specific pathogen-free (SPF) conditions under a 12-h light, 12-h dark cycle with food and water *ad libitum* at the Center for Experimental Models and Transgenic Service (CEMT, Freiburg, Germany). GF 5xFAD mice were generated via embryo transfer by Kathleen McCoy. GF heterozygous 5xFAD and WT littermates were obtained from the Clean Mouse Facility (Bern, Switzerland). In order to deplete microbiota, 5xFAD mice and littermate controls were treated orally via drinking water with a mixture of antibiotics (ABX), containing 1 mg/ml vancomycin (Hexal), 1 mg/ml cefoxitin (Santa Cruz Biotechnology), 1 mg/ml gentamicin (Sigma-Aldrich), and 1 mg/ml metronidazole (Sigma-Aldrich) for 2 months and analyzed an age of 4 months. All animal experiments were approved by the Ministry for Nature, Environment and Consumers' Protection of the State of Baden-Württemberg and were performed in accordance with the respective national, federal, and institutional regulations (permit numbers G19-02 and X16-04A).

### Histology

Histology was performed as described recently (Erny *et al*, 2015). Brains were removed and fixed in 4% phosphate-buffered formalin. Brain tissue was dissected, and parasagittal sections were embedded in paraffin before staining with Iba1 (Wako, Osaka, Japan) for microglia and CAMs. At least 3–4 parasagittal brain sections per mouse were evaluated using Bresser MikroCamLabII (Bresser, Rhede, Germany).

For immunofluorescence staining, coronal cryosections with a thickness of 25  $\mu$ m from adult brain tissue were prepared as described previously (Mezo *et al*, 2020) and incubated free-floating first with anti-Iba1 antibody (Wako, 019-19741, Osaka, Japan), for 24 h (dilution 1:500 at 4°C). Subsequently, Alexa Fluor 488-conjugated secondary antibody (Life technologies, Darmstadt, Germany) was added at a dilution of 1:500 for 24 h at 4°C. Compact A $\beta$ -plaques, as well as 1-16 A $\beta$  precursor forms, were visualized by using anti-6E10 antibody (1:1,000, 803004, BioLegend, San Diego, USA) at 4°C for 24 h, followed by incubation with corresponding conjugated secondary antibodies Alexa Fluor 568 (1:500, Life technologies) for 24 h at 4°C. DAPI was used as a nuclear stain for 10 min at RT. A $\beta$ -plaque load and density of Iba1-immunoreactive pM $\Phi$  were quantified throughout the entire hippocampus. Further cortical mM $\Phi$  and cpM $\Phi$  were assessed. Images were taken with a BZ-9000 Biorevo microscope (Keyence, Neu-Isenburg, Germany), and the number of Iba1-positive cells was determined using BZ-II Analyzer (Keyence, Neu-Isenburg, Germany).

Paraffin-embedded brains were cut sagittal into 3  $\mu$ m thin sections, and immunofluorescence labeling was performed as described previously with slight modifications (Mezo *et al*, 2020) by using following primary antibodies: anti-CD206 (1:100, MCA2235, Bio-Rad, Feldkirchen, Germany), anti-Iba1 (1:500, NB100-1028, Novus Biologicals, Wiesbaden, Germany or Wako, 019-19741, Osaka, Japan), anti-CD74 (1:200, PA5-22113, Thermo Fisher, Waltham, USA), anti-P2RY12 (1:200, AS-55043A, AnaSpec, Fremont, USA), anti-KI67 (1:200, ab15580, Abcam, Cambridge, UK), and anti-APOE (1:50, AB947, Merck, Darmstadt, Germany), upon antigen retrieval (pH 6.0 citrate) at 4°C for 24 h. Subsequently,



respective conjugated secondary antibodies Alexa Fluor 488, 568, or 647 (1:500, Life technologies) were used for 2 h at RT. Nuclei were stained with DAPI (1:10,000) for 10 min at RT. Fluorescence images were taken with BZ-9000 Biorevo microscope (Keyence). Sections were analyzed by using BZ-II Analyzer Software (Keyence). Confocal images were taken with Leica SP8 confocal laser scanning microscope (Leica, Wetzlar, Germany).

### 3D reconstruction

30  $\mu\text{m}$  parasagittal cryosections from adult brain tissue were stained with anti-Iba1 (1:500, 019-19741, Wako, Osaka, Japan), CD31 (1:200, 550274, BD Pharmingen, Heidelberg, Germany), and ER-TR7 (1:1,000, ab51824, Abcam, Cambridge, UK) for 48 hours (dilution 1:500 at 4°C), followed by Alexa Fluor 488- and 568-conjugated secondary antibody (Life technologies, Darmstadt, Germany) staining, which was added at a dilution of 1:500 overnight at 4°C, as described previously (Erny *et al*, 2015). Nuclei were counterstained with DAPI. Imaging was performed on an Olympus Fluoview 1000 confocal laser scanning microscope (Olympus, Hamburg, Germany) using a  $20 \times 0.95$  NA objective. Z stacks were done with 1.14- $\mu\text{m}$  steps in z direction, and  $1,024 \times 1,024$  pixel resolution was recorded and analyzed using IMARIS software (Bitplane, Zurich, Switzerland). At least three cortical cells were reconstructed per mouse.

### Myeloid cell isolation

To enrich the yield of CAMs, we pooled 20 mice per group. The different CNS compartments were separated, and myeloid cells were isolated as described before with slight modifications (Erny *et al*, 2015; Jordao *et al*, 2019). In short, the leptomeninges were dissected from the brain to obtain separate samples of the leptomeninges and of the parenchyma and perivascular space. All choroid plexuses were removed from the ventricles of the brain. Myeloid cells from the parenchyma and perivascular space were isolated using a 37% Percoll gradient (Sigma-Aldrich) at 800 g (4°C) from the homogenized tissue. Tissue from the choroid plexuses and leptomeninges was treated independently by mechanical dissociation through a 70- $\mu\text{m}$  cell strainer to obtain cell suspensions. Dead cells were stained using the Fixable Viability Dye eFluor 780 (1:1,000, eBioscience, San Diego, USA) followed by incubation with Fc receptor blocking antibody CD16/CD32 (BD Bioscience, Heidelberg, Germany). Afterward, cells were stained with primary antibodies directed against CD11b (M1/70), CD45 (30-F11; eBioscience, San Diego, USA), CD206 (C068C2), B220 (RA3-6B2; BioLegend), CD3 (ASP34-2), Ly6C (AL-21), and Ly6G (1A8; BD Bioscience, Heidelberg, Germany) with a dilution of 1:200 at 4°C for 30 min. Viable single cells from  $n \geq 5$  animals per condition were pooled and sorted with a MoFlo Astrios (Beckman Coulter, Krefeld, Germany) into 384-well plates and further processed.

### Single-cell RNA-seq analysis

Samples were processed using the mCel-Seq2 protocol (Herman *et al*, 2018). 28 libraries were sequenced in batches of eight libraries with 192 cells each per lane on an Illumina HiSeq 3000 sequencing system (pair-end multiplexing run) at a depth of  $\sim 130,000$ – $200,000$  reads per cell. Features with a correlation coefficient of  $> 0.65$  with low-quality cell marker *Kcnq1ot1* were excluded from analysis

(Grun *et al*, 2016). 2,815 cells containing more than 500 features (cell numbers per condition—SPF: 1,142; GF: 1,673; cell numbers per compartment—microglia: 830, cpM $\Phi$ : 489, pvM $\Phi$ : 942, mM $\Phi$ : 554) were analyzed using Seurat version 3 (Stuart *et al*, 2019). Doublet detection was performed with an estimated multiplet rate of 2.5% on a Seurat object with all cells using the DoubletFinder R package version 2.0.3 leading to a final dataset of 2,745 cells. A total of 19,488 gene loci were quantified with a median of 1,489 features per cell  $\pm 735.44$  (S.D.). Data analysis was performed using the Seurat version 3 algorithm (Herman *et al*, 2018) using the SCTransform workflow with default parameters on the first 15 principal components of the data. The resolution parameter for the FindClusters function was chosen at 1.2 after visual inspection of the resulting clustering tree using the clustree R package version 0.4.3 (<https://github.com/lazappi/clustree>). Cluster markers for heatmap visualizations were obtained using the FindAllMarkers Seurat function. Direct comparisons of microglia and CAMs from GF and SPF mice were conducted using the FindMarkers Seurat function.

### Cluster enrichment analysis

Enrichment analysis for GF or SPF-derived cells in a cluster was done using a hypergeometric test implemented in R under the phyper function. This test considers the number of cells from a condition in per cluster with respect to all cells from this condition in the dataset, all cells from the second condition in the dataset and the number of cells in each cluster. The *P*-value returns the probability that number *n* or more cells from a condition could be found in a given cluster by chance. Probabilities of  $< 0.05$  were considered statistically significant. Multiple testing correction was achieved using the Benjamini–Hochberg method.

### Gene ontology analysis

Enrichment of gene ontology (GO) term analysis was analyzed using the clusterProfiler R package version 4.0.5 (Yu *et al*, 2012). Differentially expressed cluster marker genes were used as input gene lists. All quantified genes in the dataset are used as background genes.

### Pseudotime analysis of single-cell transcriptomes

The StemID2 (contained within RaceID version 0.2.3) and FateID version 0.2.0 packages were used for pseudotime trajectory analysis of the single-cell RNA-seq with default settings (Grun *et al*, 2016; Herman *et al*, 2018). After construction of a lineage tree using the nearest neighbor mode (nmode=TRUE) with default parameters of StemID2, a list of significant links was chosen for each cell type in question. A filtered gene expression matrix was used as input for the pseudotime gene expression analysis of cells along the list of selected links. Lowly expressed genes were removed with the filterset FateID function. The getsom and procsom FateID functions grouped genes with similar gene expression profiles into modules on a self-organizing map. Smoothed z-scores of the genes in these modules were visualized.

### LCMV challenge

Lymphocytic choriomeningitis virus strain WE was propagated and titrated as plaque-forming units (PFU) on L929 cells as described

before (Herz *et al.*, 2009). PFU were multiplied by the factor 10 to be converted into infectious units (IU). Mice were infected by intracerebral inoculation of  $10^3$  IU into the right hemisphere.

### Ex vivo A $\beta$ phagocytosis assay

Mice were injected intraperitoneally with methoxy-X-04 (Tocris) (10 mg/kg bodyweight), a fluorescent congo red derivative, in a DMSO/PBS mixture as described previously (Mezo *et al.*, 2020). After 3 h, hippocampi were collected and pvM $\Phi$  were assessed as CD11b<sup>+</sup>CD45<sup>hi</sup> cells. Percentage of methoxy-XO-4-positive pvM $\Phi$  were determined by flow cytometry using a FACS Canto II (BD Bioscience) and analyzed with FlowJo software (Tree Star).

### Statistical analysis

Statistical analysis was performed using GraphPad Prism (GraphPad Software, version 5.0, La Jolla, USA). Tabular data were processed using the tidyverse suite of packages (Wickham & Wickham, 2017) and visualized in the R programming environment version 4.1.0 (R Core Team, 2013) using the ggplot2 package version 3.3.5 (Wickham, 2016).

All data were tested for normality applying the Shapiro–Wilk normality test. If normality was given, an unpaired *t*-test, one-way ANOVA followed by Tukey's *post hoc* comparison test or two-way ANOVA followed by Tukey's *post hoc* comparison test was applied, respectively. Differences were considered significant when *P*-value < 0.05. To obtain unbiased data, experimental mice were all processed together, and cell quantifications were performed blinded by two scientists independently and separately.

## Data and software availability

Raw and processed single cell RNA-seq data including the metadata and Seurat objects are available at Gene Expression Omnibus (GEO: GSE178956). The code book for the present study is available under: [https://github.com/rsankowski/sankowski\\_et\\_al\\_murine\\_CAMs](https://github.com/rsankowski/sankowski_et_al_murine_CAMs).

**Expanded View** for this article is available online.

### Acknowledgements

We thank Eileen Barleon, Maria Oberle, and Tina el Gaz for excellent technical assistance. We are grateful to Jan Bodinek-Wersing for cell sorting. We are grateful to Ulrike Karow for assisting with LCMV treatment. We thank Dominic Grün and Sagar, MPI IE Freiburg, for their generous support with scRNA-seq. ASF and recolonized ASF mice were kindly provided by Bärbel Stecher (Max-von-Pettenkofer Institute, LMU Munich, German Center for Infection Research). FFAR2-deficient mice and wild-type controls were kindly provided by Wendy Garrett (Harvard School of Public Health, Boston, MA, USA). R.S. was funded by the Else Kröner Fresenius Foundation and the Berta-Ottenstein-Programme for Clinician Scientists, Faculty of Medicine, University of Freiburg. The single-cell analyses were conducted within the Single-cell Omics Platform. DE and TBL were supported by the Deutsche Forschungsgemeinschaft (DFG, German Research Foundation) (CRC/TRR167), and DE was further supported by the Berta-Ottenstein-Programme for Advanced Clinician Scientists, Faculty of Medicine, University of Freiburg. Open Access funding enabled and organized by Projekt DEAL.

### Author contributions

RS, JA, CM, ALHA, VF, TBL, and DE performed the experiments. RS analyzed the single-cell RNA-sequencing data. OU performed infection with LCMV. MGA an AJM bred GF animals and performed SCFA treatment. TBU provided animals. All authors read and approved the manuscript. RS and DE wrote the manuscript and prepared the figures. DE initiated and supervised the project.

### Conflict of interest

The authors declare that they have no conflict of interest.

## References

- Amit I, Winter DR, Jung S (2016) The role of the local environment and epigenetics in shaping macrophage identity and their effect on tissue homeostasis. *Nat Immunol* 17: 18–25
- Baruch K, Deczkowska A, David E, Castellano JM, Miller O, Kertser A, Berkutzki T, Barnett-Itzhaki Z, Bezalel D, Wyss-Coray T *et al* (2014) Aging. Aging-induced type I interferon response at the choroid plexus negatively affects brain function. *Science* 346: 89–93
- Brioschi S, Zhou Y, Colonna M (2020) Brain parenchymal and extraparenchymal macrophages in development, homeostasis, and disease. *J Immunol* 204: 294–305
- Butovsky O, Jedrychowski MP, Moore CS, Cialic R, Lanser AJ, Gabriely G, Koeglsperger T, Dake B, Wu PM, Doykan CE *et al* (2014) Identification of a unique TGF- $\beta$ -dependent molecular and functional signature in microglia. *Nat Neurosci* 17: 131–143
- Chu C, Murdock MH, Jing D, Won TH, Chung H, Kressel AM, Tsaava T, Addorisio ME, Putzel GG, Zhou L *et al* (2019) The microbiota regulate neuronal function and fear extinction learning. *Nature* 574: 543–548
- Conrad ML, Ferstl R, Teich R, Brand S, Blümer N, Yildirim AÖ, Patrascan CC, Hanuszkiewicz A, Akira S, Wagner H *et al* (2009) Maternal TLR signaling is required for prenatal asthma protection by the nonpathogenic microbe *Acinetobacter lwoffii* F78. *J Exp Med* 206: 2869–2877
- Cui J, Shipley FB, Shannon ML, Alturkistani O, Dani N, Webb MD, Sugden AU, Andermann ML, Lehtinen MK (2020) Inflammation of the embryonic choroid plexus barrier following maternal immune activation. *Dev Cell* 55: 617–628
- Ding J, Adiconis X, Simmons SK, Kowalczyk MS, Hession CC, Marjanovic ND, Hughes TK, Wadsworth MH, Burks T, Nguyen LT *et al* (2020) Systematic comparison of single-cell and single-nucleus RNA-sequencing methods. *Nat Biotechnol* 38: 737–746
- Erny D, Hrabě de Angelis AL, Jaitin D, Wieghofer P, Staszewski O, David E, Keren-Shaul H, Mhlahkoiv T, Jakobshagen K, Buch T *et al* (2015) Host microbiota constantly control maturation and function of microglia in the CNS. *Nat Neurosci* 18: 965–977
- Erny D, Prinz M (2020) How microbiota shape microglial phenotypes and epigenetics. *Glia* 68: 1655–1672
- Faraco G, Sugiyama Y, Lane D, Garcia-Bonilla L, Chang H, Santisteban MM, Racchumi G, Murphy M, Van Rooijen N, Anrather J *et al* (2016) Perivascular macrophages mediate the neurovascular and cognitive dysfunction associated with hypertension. *J Clin Invest* 126: 4674–4689
- Garzetti D, Brugiroux S, Bunk B, Pukall R, McCoy KD, Macpherson AJ, Stecher B (2017) High-quality whole-genome sequences of the oligo-mouse-microbiota bacterial community. *Genome Announc* 5: e00758-17
- Geirsdottir L, David E, Keren-Shaul H, Weiner A, Bohlen SC, Neuber J, Balic A, Giladi A, Sheban F, Dutertre C-A *et al* (2019) Cross-species single-cell

- analysis reveals divergence of the primate microglia program. *Cell* 179: 1609–1622
- Giannoni P, Arango-Lievano M, Neves ID, Rousset MC, Baranger K, Rivera S, Jeanneteau F, Claeysen S, Marchi N (2016) Cerebrovascular pathology during the progression of experimental Alzheimer's disease. *Neurobiol Dis* 88: 107–117
- Goldmann T, Wieghofer P, Jordão MJC, Prutek F, Hagemeyer N, Frenzel K, Amann L, Staszewski O, Kierdorf K, Krueger M et al (2016) Origin, fate and dynamics of macrophages at central nervous system interfaces. *Nat Immunol* 17: 797–805
- Gosselin D, Link VM, Romanoski C, Fonseca G, Eichenfield D, Spann N, Stender J, Chun H, Garner H, Geissmann F et al (2014) Environment drives selection and function of enhancers controlling tissue-specific macrophage identities. *Cell* 159: 1327–1340
- Grün D, Muraro M, Boisset J-C, Wiebrands K, Lyubimova A, Dharmadhikari G, van den Born M, van Es J, Jansen E, Clevers H et al (2016) De novo prediction of stem cell identity using single-cell transcriptome data. *Cell Stem Cell* 19: 266–277
- Hagemeyer N, Hanft KM, Akritidou MA, Unger N, Park ES, Stanley ER, Staszewski O, Dimou L, Prinz M (2017) Microglia contribute to normal myelinogenesis and to oligodendrocyte progenitor maintenance during adulthood. *Acta Neuropathol* 134: 441–458
- Hawkes CA, McLaurin J (2009) Selective targeting of perivascular macrophages for clearance of beta-amyloid in cerebral amyloid angiopathy. *Proc Natl Acad Sci USA* 106: 1261–1266
- Hawkes CA, Jayakody N, Johnston DA, Bechmann I, Carare RO (2014) Failure of perivascular drainage of beta-amyloid in cerebral amyloid angiopathy. *Brain Pathol* 24: 396–403
- Heneka MT, Golenbock DT, Latz E (2015) Innate immunity in Alzheimer's disease. *Nat Immunol* 16: 229–236
- Herman JS, Sagar, Grün D (2018) FateID infers cell fate bias in multipotent progenitors from single-cell RNA-seq data. *Nat Methods* 15: 379–386
- Herz J, Pardo J, Kashkar H, Schramm M, Kuzmenkina E, Bos E, Wiegmann K, Wallich R, Peters PJ, Herzig S et al (2009) Acid sphingomyelinase is a key regulator of cytotoxic granule secretion by primary T lymphocytes. *Nat Immunol* 10: 761–768
- Herz J, Filiano AJ, Smith A, Yogev N, Kipnis J (2017) Myeloid cells in the central nervous system. *Immunity* 46: 943–956
- Hoeffel G, Ginhoux F (2018) Fetal monocytes and the origins of tissue-resident macrophages. *Cell Immunol* 330: 5–15
- Jordão MJC, Sankowski R, Brendecke SM, Sagar, Locatelli G, Tai Y-H, Tay TL, Schramm E, Armbruster S, Hagemeyer N et al (2019) Single-cell profiling identifies myeloid cell subsets with distinct fates during neuroinflammation. *Science* 363: eaat7554
- Kawai T, Akira S (2009) The roles of TLRs, RLRs and NLRs in pathogen recognition. *Int Immunol* 21: 317–337
- Keren-Shaul H, Spinrad A, Weiner A, Matcovitch-Natan O, Dvir-Szternfeld R, Ulland TK, David E, Baruch K, Lara-Astasio D, Toth B et al (2017) A unique microglia type associated with restricting development of Alzheimer's disease. *Cell* 169: 1276–1290
- Kharchenko PV, Silberstein L, Scadden DT (2014) Bayesian approach to single-cell differential expression analysis. *Nat Methods* 11: 740–742
- Khosravi A, Yanez A, Price JG, Chow A, Merad M, Goodridge HS, Mazmanian SK (2014) Gut microbiota promote hematopoiesis to control bacterial infection. *Cell Host Microbe* 15: 374–381
- Kierdorf K, Masuda T, Jordao MJC, Prinz M (2019) Macrophages at CNS interfaces: ontogeny and function in health and disease. *Nat Rev Neurosci* 20: 547–562
- Kim J-S, Kolesnikov M, Peled-Hajaj S, Scheyltjens I, Xia Y, Trzebanski S, Haimon Z, Shemer A, Lubart A, Van Hove H et al (2021) A binary Cre transgenic approach dissects microglia and CNS border-associated macrophages. *Immunity* 54: 176–190
- Krasemann S, Madore C, Cialic R, Baufeld C, Calcagno N, El Fatimy R, Beckers L, O'Loughlin E, Xu Y, Fanek Z et al (2017) The TREM2-APOE pathway drives the transcriptional phenotype of dysfunctional microglia in neurodegenerative diseases. *Immunity* 47: 566–581
- Lavin Y, Winter D, Blecher-Gonen R, David E, Keren-Shaul H, Merad M, Jung S, Amit I (2014) Tissue-resident macrophage enhancer landscapes are shaped by the local microenvironment. *Cell* 159: 1312–1326
- Mező C, Dokalis N, Mossad O, Staszewski O, Neuber J, Yilmaz B, Schnepf D, de Agüero MG, Ganal-Vonarburg SC, Macpherson AJ et al (2020) Different effects of constitutive and induced microbiota modulation on microglia in a mouse model of Alzheimer's disease. *Acta Neuropathol Commun* 8: 119
- Mildner A, Schlevogt B, Kierdorf K, Bottcher C, Erny D, Kummer MP, Quinn M, Bruck W, Bechmann I, Heneka MT et al (2011) Distinct and non-redundant roles of microglia and myeloid subsets in mouse models of Alzheimer's disease. *J Neurosci* 31: 11159–11171
- Mildner A, Schonheit J, Giladi A, David E, Lara-Astiaso D, Lorenzo-Vivas E, Paul F, Chappell-Maor L, Priller J, Leutz A et al (2017) Genomic characterization of murine monocytes reveals C/EBPbeta transcription factor dependence of Ly6C(-) cells. *Immunity* 46: 849–862
- Mrdjen D, Pavlovic A, Hartmann FJ, Schreiner B, Utz SG, Leung BP, Lelios I, Heppner FL, Kipnis J, Merkler D et al (2018) High-dimensional single-cell mapping of central nervous system immune cells reveals distinct myeloid subsets in health, aging, and disease. *Immunity* 48: 599
- Nagai Y, Shimazu R, Ogata H, Akashi S, Sudo K, Yamasaki H, Hayashi S, Iwakura Y, Kimoto M, Miyake K (2002) Requirement for MD-1 in cell surface expression of RP105/CD180 and B-cell responsiveness to lipopolysaccharide. *Blood* 99: 1699–1705
- Oakley H, Cole SL, Logan S, Maus E, Shao P, Craft J, Guillozet-Bongaarts A, Ohno M, Disterhoft J, Van Eldik L et al (2006) Intraneuronal beta-amyloid aggregates, neurodegeneration, and neuron loss in transgenic mice with five familial Alzheimer's disease mutations: potential factors in amyloid plaque formation. *J Neurosci* 26: 10129–10140
- Prinz M, Erny D, Hagemeyer N (2017) Ontogeny and homeostasis of CNS myeloid cells. *Nat Immunol* 18: 385–392
- R Core Team (2013) *R: A language and environment for statistical computing*. <https://www.R-project.org/>
- Sampson TR, Debelius JW, Thron T, Janssen S, Shastri GG, Ilhan ZE, Challis C, Schretter CE, Rocha S, Gradinaru V et al (2016) Gut microbiota regulate motor deficits and neuroinflammation in a model of Parkinson's disease. *Cell* 167: 1469–1480
- Sankowski R, Böttcher C, Masuda T, Geirsdottir L, Sagar, Sindram E, Seredenina T, Muhs A, Scheiwe C, Shah MJ et al (2019) Mapping microglia states in the human brain through the integration of high-dimensional techniques. *Nat Neurosci* 22: 2098–2110
- Shiple FB, Dani N, Xu H, Deister C, Cui J, Head JP, Sadegh C, Fame RM, Shannon ML, Flores VI et al (2020) Tracking calcium dynamics and immune surveillance at the choroid plexus blood-cerebrospinal fluid interface. *Neuron* 108: 623–639
- Stecher B, Chaffron S, Käppli R, Hapfelmeier S, Friedrich S, Weber TC, Kirundi J, Suar M, McCoy KD, von Mering C et al (2010) Like will to like: abundances of closely related species can predict susceptibility to intestinal colonization by pathogenic and commensal bacteria. *PLoS Pathog* 6: e1000711

- Stuart T, Butler A, Hoffman P, Hafemeister C, Papalexi E, Mauck 3rd WM, Hao Y, Stoeckius M, Smibert P, Satija R (2019) Comprehensive integration of single-cell data. *Cell* 177: 1888–1902
- Uchimura Y, Wyss M, Brugiroux S, Limenitakis JP, Stecher B, McCoy KD, Macpherson AJ (2016) Complete genome sequences of 12 species of stable defined moderately diverse mouse microbiota 2. *Genome Announc* 4: e00951-16
- Ueno M, Fujita Y, Tanaka T, Nakamura Y, Kikuta J, Ishii M, Yamashita T (2013) Layer V cortical neurons require microglial support for survival during postnatal development. *Nat Neurosci* 16: 543–551
- Utz SG, See P, Mildnerberger W, Thion MS, Silvin A, Lutz M, Ingelfinger F, Rayan NA, Lelios I, Buttgerit A et al (2020) Early fate defines microglia and non-parenchymal brain macrophage development. *Cell* 181: 557–573
- Van Hove H, Martens L, Scheyltjens I, De Vlaminck K, Pombo Antunes AR, De Prijck S, Vandamme N, De Schepper S, Van Isterdael G, Scott CL et al (2019) A single-cell atlas of mouse brain macrophages reveals unique transcriptional identities shaped by ontogeny and tissue environment. *Nat Neurosci* 22: 1021–1035
- Wickham H (2016) *ggplot2: elegant graphics for data analysis*. New York: Springer-Verlag
- Wickham H, Wickham MH (2017) *Package tidyverse*. Easily Install and Load the 'Tidyverse
- Yu G, Wang LG, Han Y, He QY (2012) clusterProfiler: an R package for comparing biological themes among gene clusters. *OMICS* 16: 284–287
- Zeisel A, Munoz-Manchado AB, Codeluppi S, Lonnerberg P, La Manno G, Jureus A, Marques S, Munguba H, He L, Betscholtz C et al (2015) Brain structure. Cell types in the mouse cortex and hippocampus revealed by single-cell RNA-seq. *Science* 347: 1138–1142
- Zhang D, Chen G, Manwani D, Mortha A, Xu C, Faith JJ, Burk RD, Kunisaki Y, Jang J-E, Scheiermann C et al (2015) Neutrophil ageing is regulated by the microbiome. *Nature* 525: 528–532
- Zhou J, Tang PC, Qin L, Gayed PM, Li W, Skokos EA, Kyriakides TR, Pober JS, Tellides G (2010) CXCR3-dependent accumulation and activation of perivascular macrophages is necessary for homeostatic arterial remodeling to hemodynamic stresses. *J Exp Med* 207: 1951–1966



**License:** This is an open access article under the terms of the Creative Commons Attribution-NonCommercial-NoDeriv License, which permits use and distribution in any medium, provided the original work is properly cited, the use is non-commercial and no modifications or adaptations are made.